POLITECNICO DI TORINO

Master's Degree Course in
MATERIALS ENGINEERING FOR INDUSTRY 4.0

College of Chemical and Materials Engineering

Master's Thesis

3D printing by photopolymerisation of biobased monomers with conductive fillers

Supervisor: **Candidate:**

Prof. Marco Sangermano   Alberto Cellai

October 2024

Index

Politecnico di Torino

1 Introduction

As highlighted by the UN's 2030 Agenda for Sustainable Development, achieving sustainable development is one of the most important but at the same time complicated tasks of the current historical period. One of the main reasons for the existence of this agenda, as well as one of the main goals, is to try to limit and reduce climate change, which entails multiple challenges, including ending dependence on fossil fuels, reducing greenhouse gas emissions and, in general, minimizing the carbon footprint of the population and production processes. To address these issues, innovations in materials science play an important role in the creation of new materials that support and participate in a circular economy, promoting sustainable manufacturing. In this field, bio-based polymers represent natural alternatives to fossil-based plastics, offering a promising path towards more sustainable production and use. [1]

Furthermore, still focusing on the industrial world of plastics, the type of process used to develop polymeric objects must also be considered, naturally favouring environmentally friendly methods. UV technology, for the consolidation of polymers, is among the most sustainable techniques due to its low emission of volatile organic compounds (VOC), high efficiency and lower energy consumption compared to heat-based processes. Today, this technology is widely used in the production of adhesives, coatings, inks and in the dental sector.

More recently, UV curing has started to be exploited for additive manufacturing (AM), leading to several advantages that contribute to the reduction of material and energy waste. Firstly, the use of material occurs in a concealed manner, placing it only where required, avoiding or drastically reducing the creation of scraps. Secondly, the possibility of using materials from bio-renewable sources in the AM technologies allows for a gradual move away from polymers derived from fossil fuels, addressing one of the main challenges mentioned above. [2]

Regarding this last topic, of particular interest are the commercially available polyglycerol-based acrylic monomers produced by SYntech SA Series of Sakamoto Yakuhin Kogyo Co. These monomers are important because the acrylic groups enhance and enable UV polymerisation, which requires minimal energy and time at room temperature. Of the various AM techniques, VAT polymerization methods has proven to be the most suitable method for handling liquid monomers such as those shown.

Additionally, a factor of high importance is making these new materials unique and attractive on the market, to promote their purchase and use by a wide variety of companies. To do this, the range of application fields for these resins should be increased as much as possible. One possible way is to enhance these 3D-printed structures with additional functionalities, such as electrical conductivity, which is still an area of ongoing development. A valid approach to achieve this is to disperse conductive fillers within the polymer matrix, in this way, by incorporating carbon or metal-based materials into the printing resins, it is possible to create 3D-printed components that exhibit significant electrical conductivity.

One of the possible applications of this technology is in the medical field, particularly for thermotherapy treatments. By exploiting the Joule effect, in which heat is produced by a flowing current, 3D printed conductive materials can be used to create customized devices that deliver localized heat directly to specific areas of the body. This could be particularly beneficial for treating

Politecnico di Torino

conditions such as muscle pain, arthritis or even targeted cancer treatments, where precise temperature control is at the heart of the mechanism. [3][4]

Beyond the medical sector, the use of conductive fillers in 3D printed structures has significant potential in various industrial applications. For example, in electronics, it could lead to the production of custom-designed conductive pathways or components integrated into larger systems.

1.1 Overview on 3D printing technologies

Unlike traditional subtractive manufacturing methods, which involve cutting away and generally remove material from a solid block to create an object, additive manufacturing concept relies on the rule of adding material only where necessary, based on a 3D computerized model. This method not only reduces waste but also enables the creation of very complex geometries that would be challenging or even impossible to achieve with conventional techniques.

The roots of 3D printing can be traced back to the 1980s when Charles Hull invented, patented and commercialized the first 3D printing process, stereolithography. Starting from this point, additive manufacturing technologies have seen phenomenal growth, by transitioning from a niche prototyping tools to a valuable manufacturing solutions on the industrial scale. Additionally, the range of materials that can now be used in 3D printing methods is considerably increased from the early development period, including conventional thermoplastics and thermoset polymers, metals, and even ceramics, making 3D printing suitable for a very wide range of applications. In particular, AM technologies are particularly well-suited for mass customization, allowing manufacturers to produce tailor-made products at scale without the need for extensive retooling. This capability is very appreciated in industries such as healthcare, where customized medical implants and prosthetics can be produced quickly and accurately. Additionally, in the automotive and aerospace sectors, 3D printing enables the production of lightweight and complex components that improve performance and fuel efficiency, by exploiting topological design and optimization. Furthermore, 3D printing community is an open-source one, enabling hobbyists and small businesses to create and share innovative designs, fostering a collaborative environment for technological advancement.

According to the ASTM Standard F2792, 3D printing technologies are categorized into seven distinct groups. [5] [6]

1.1.1 Binder Jetting

Binder jetting is a rapid prototyping method where a liquid binder is selectively deposited to permit powder particles to stay linked together. This technique involves the use of a chemical binder sprayed onto a powder bed to form layers, such as shown in Figure 1.1. Binder jetting is ideal for producing casting patterns, raw sintered products, and other large-scale items, particularly from materials like sand, which often require no additional processing. It is a straightforward, fast, and cost-effective process capable of printing large objects and using various materials, including metals, sands, polymers, hybrids, and ceramics. [7]
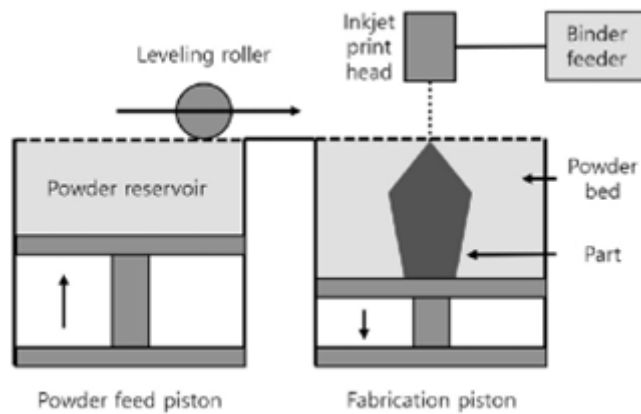
Politecnico di Torino

Figure 1.1: schematic of binder jetting technique

1.1.2 Directed Energy Deposition (DED)

Directed energy deposition is a more complex 3D printing process often used to repair or add material to existing components. It offers high control over grain structure, resulting in high-quality outputs. This process typically uses metals and metal-based hybrids in wire or powder form but can also work with ceramics and polymers. In particular, this technology is gaining attention in sectors like tooling, transportation, aerospace, and oil and gas due to its scalability and versatile capabilities.

Examples of DED technologies include laser deposition, such as showed in Figure 1.2, and Laser Engineered Net Shaping (LENS). [8]
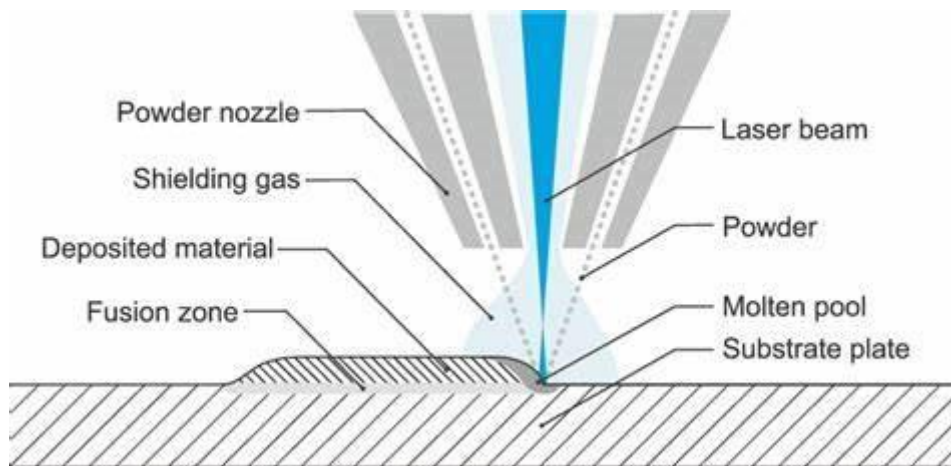

Figure 1.2: refiguration of a DED system

1.1.3 Material Extrusion

Material extrusion-based 3D printing technologies are widely used for its low cost and ability to print multi-material and multi-color objects, basically by extruding material through a nozzle to build objects layer by layer. Fused Deposition Modeling (FDM), developed in the early 1990s, is a prominent example, visible in Figure 1.3. In FDM, thermoplastic-based filaments are heated to a semi-liquid state and extruded in fine beads along the desired path. Support structures made of removable material can also be deposited where needed to support the growing object. [9]
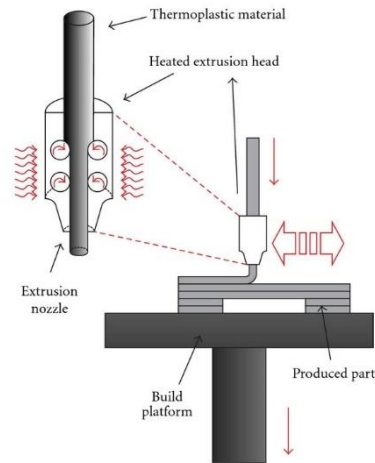

Figure 1.3: schematic of a FDM setup

1.1.4 Material Jetting

Material jetting, as defined by ASTM Standards, involves selectively depositing droplets of build material. In this process, showed in Figure 1.4, a printhead dispenses photosensitive material that solidifies under ultraviolet (UV) light, building parts layer by layer. Material jetting offers high dimensional accuracy and smooth surface finishes and can utilize various materials such as polymers, ceramics, composites, biologicals, and hybrids. [10]
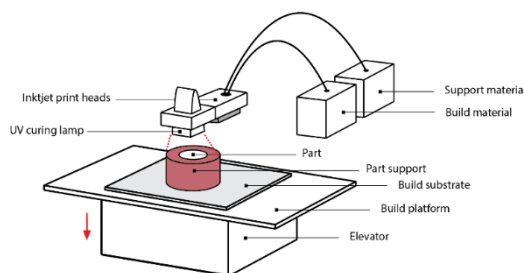

Figure 1.4: Material jetting process

1.1.5 Powder Bed Fusion

Powder bed fusion encompasses techniques like Electron Beam Melting (EBM), Selective Laser Sintering (SLS), and Selective Heat Sintering (SHS). These methods use an electron beam or laser to melt or fuse powder materials. SLS, visible in Figure 1.5, was developed by Carl Deckard in 1987, and it is noted for its speed, accuracy, and ability to create objects from metal, plastic, and ceramic powders. On the other hand, SHS uses a thermal print head to melt thermoplastic powder, while EBM employs an electron beam as energy source to heat and melt metallic and ceramic materials mainly. [11]
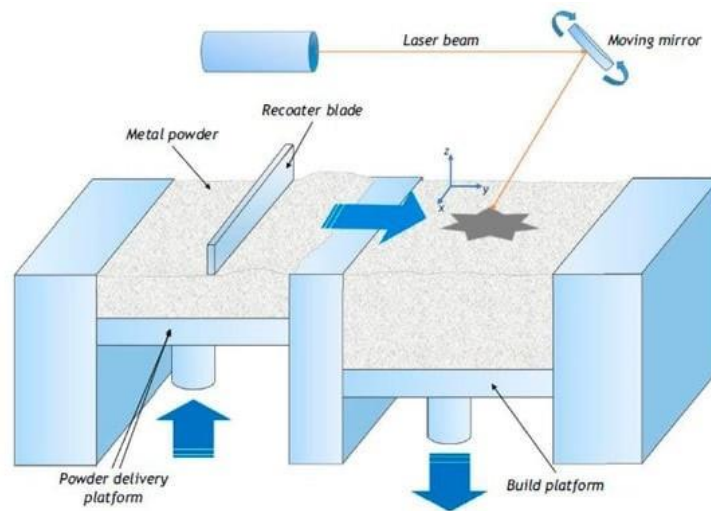

Figure 1.5: SLS setup

1.1.6 Sheet Lamination

As defined by ASTM, sheet lamination involves bonding sheets of material to create objects. Examples include Laminated Object Manufacturing (LOM) and Ultrasound Additive Manufacturing (UAM). These processes are advantageous for producing full-color prints, handling materials easily, and recycling excess material. In particular, LOM is known for its capability to manufacture quite complex geometrical parts at a lower cost and with less operational time with respect to other AM methods. As visible from Figure 1.6, it is based on layer-by-layer cutting and lamination of sheets or rolls of materials. Successive layers are cut precisely using a cutter or laser and are then bonded together. On the other hand, UAM uses ultrasounds to merge layers of metal from foil stock. [12]
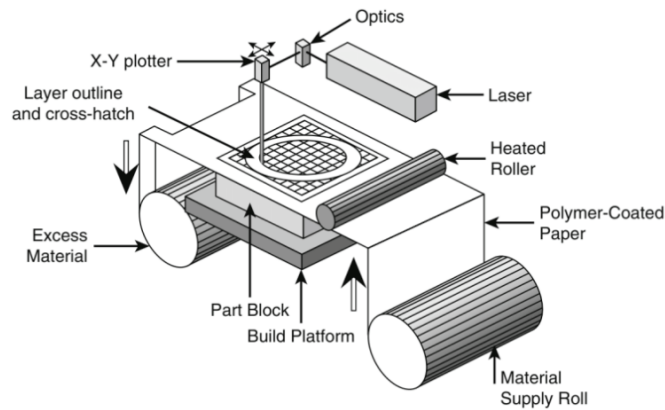
Figure 1.6: schematic of LOM

1.1.7 Vat Photopolymerization

Vat photopolymerization, frequently used in 3D printing, involves curing photo-reactive polymers using lasers, light, or UV sources. Techniques like Stereolithography (SLA) and Digital Light Processing (DLP) fall under this category. Precisely, SLA uses a laser to cure liquid resin, as visible from Figure 1.7, while DLP employs a conventional light source and liquid crystal display panel for faster processing. Key parameters include exposure time, wavelength, and power supply. This method is suitable for producing high-detail, premium-quality products. [13]
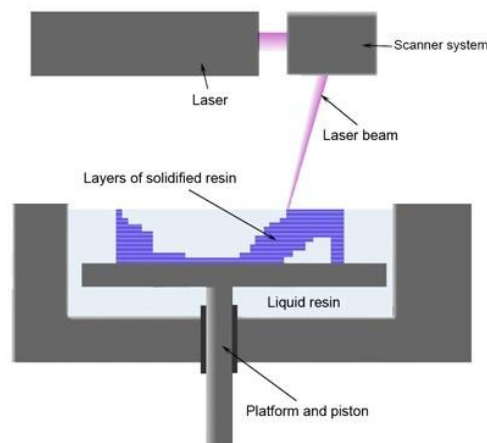

Figure 1.7: representation of SLA technology

1.2 VAT polymerization technologies

In this paragraph the state of the art of VAT polymerization methods will be reported more in depth.

As already mentioned, VAT polymerization is an additive manufacturing technique where a liquid photopolymer in a vat is cured into solid forms using a light source. The vat holds a mixture of monomers and a photoinitiator, correctly dissolved and homogenized. When exposed to light, the photoinitiator activates, causing the monomers to form long polymer chains.

There are several key methods within VAT polymerization, the most commercialized ones are stereolithography (SLA) and digital light processing (DLP), as already previously reported. However, more advanced techniques like continuous liquid interface production (CLIP), two-photon polymerization (2PP), and computed axial lithography (CAL) have also been developed in more recent years. [14]

1.2.1 SLA

Stereolithography (SLA) is one of the earliest and most established forms of VAT polymerization technique, utilizing a UV laser to selectively cure liquid photopolymer resin. This process involves the laser tracing the pattern of each layer on the resin's surface, solidifying it point by point. After a layer is solidified, the build platform moves vertically to allow the next layer of resin to be exposed and cured. There are two main configurations for SLA: top-down and bottom-up. In the top-down configuration, visible in Figure 1.8, the laser is positioned above the vat, and the platform lowers into the resin. This approach can lead to challenges such as resin disturbance when the platform moves, which can affect efficiency and precision. Gravity controls the layer thickness, often necessitating a levelling bar for improved accuracy. In contrast, the bottom-up configuration places the light source below the vat, shining and passing through a transparent bottom layer, as visible from Figure 1.9. The platform starts near the bottom of the VAT (at an height equal to the thickness of the first layer) and moves upward, reducing resin disturbance, oxygen exposure, and allowing for finer control over layer thickness through precise platform movement. This configuration also requires less resin and permits higher vertical resolution, making it a more efficient and controlled method overall. [15] [16]
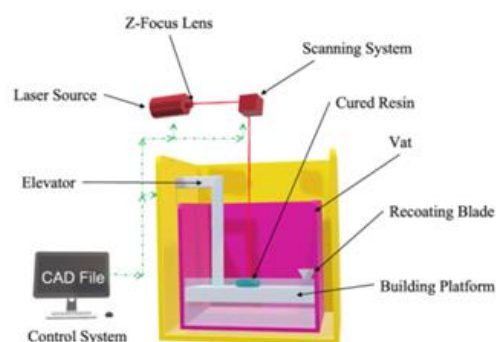

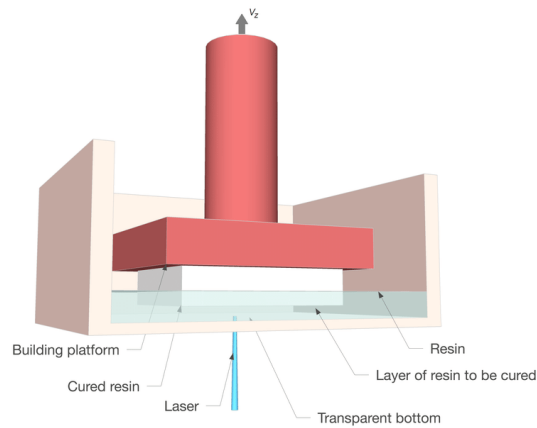*Figure 1.8: Top-Down configuration for SLA technology*

Figure 1.9: Bottom-Up setup for SLA

1.2.2 DLP

Digital Light Processing (DLP) shares similarities with SLA but employs a different light projection system. Instead of using a laser, DLP uses a Digital Mirror Device (DMD) or a Liquid Crystal Display (LCD) to project and expose entire layers onto the resin at once. As showed in Figure 1.10, this system reflects light in a manner that exposes and cures the entire layer simultaneously, significantly speeding up the process compared to the point-by-point curing of SLA. Like the bottom-up SLA, DLP also benefits from reduced oxygen inhibition due to the configuration where the light source is positioned below the vat. The resolution in DLP is determined by the pixel matrix of the DMD or LCD, meaning the quality of the printed object is directly related to the resolution of the projected light image. This allows DLP to be able to produce detailed and accurate prints rapidly, making it advantageous for applications where speed and detail are both crucial, basically by moving to a very dense pixel matrix. [17]
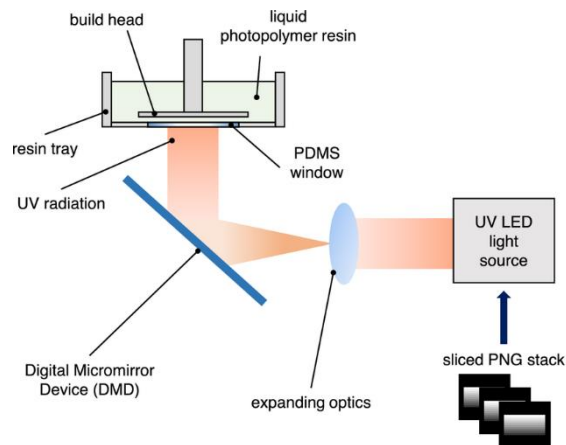

Figure 1.10: Schematic of a DLP apparatus

1.2.3 CLIP

CLIP represents an advancement over traditional DLP techniques by introducing a continuous build process. In CLIP, digital projection with LEDs is used, and the bottom of the vat is replaced with a transparent, oxygen-permeable material. This creates a "dead zone" where a thin layer of resin remains liquid due to oxygen inhibition, preventing it from curing. As the resin flows continuously at the interface between the solidified part and the bottom of the vat, the build platform moves upward in a continuous manner rather than layer by layer. This significantly accelerates the printing process and eliminates the stepwise layering effect, resulting in smoother surfaces and faster production times. A representation of the process is visible in Figure 1.11. [18]
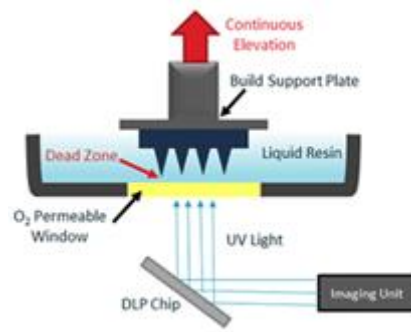

Figure 1.11: representation of CLIP technology

1.2.4 2PP

Two-Photon Polymerization (2PP) is a sophisticated technique that uses a femtosecond laser capable of emitting extremely short and high-frequency pulses. This laser induces photopolymerization by causing the near-simultaneous absorption of two photons in a highly localized volume of resin. The process allows for the creation of very fine structures with resolutions around 100 nm. The high precision of 2PP makes it ideal for fabricating intricate microstructures, though it is limited by the small build volume, typically up to 1 cubic centimeter. [19]

1.2.5 CAL

Computed Axial Lithography (CAL), visible in Figure 1.12, is one of the newest developments in VAT polymerization, utilizing a revolutionary volumetric approach to create 3D objects. In fact, instead of building layer by layer, CAL illuminates a rotating volume of photosensitive resin with a series of 2D images from multiple angles. The intersecting light patterns cure the resin into the desired shape in a single, continuous process. This technique achieves high-speed production and avoids the "stair-step" effect common in layer-by-layer methods, offering a smoother finish. However, while CAL can produce large-scale structures quickly, its overall resolution is somewhat limited compared to other methods, typically on the order of millimeters. [20]
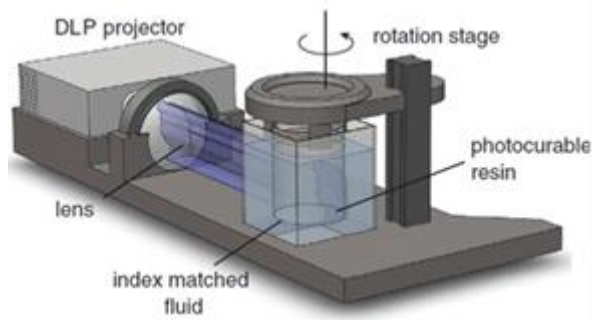
Figure 1.12: Schematic of CAL method

Post-processing for all these methods typically involves washing the printed part in a solvent bath, like isopropyl alcohol, and further curing (post-curing step) with UV light to enhance mechanical properties of the final object.

Each method balances speed, resolution, and build volume differently. In fact, 2PP excels in high resolution but with small build sizes, while CLIP and CAL are faster and can handle larger volumes, with the drawback of lower resolution. Overall, the fastest techniques are CLIP and CAL, while the highest resolution practicable techniques are SLA and DLP.

The adverse relation between the feature size and the printing area for vat photopolymerization 3D-printing technologies is displayed in Figure 1.13. Increasing the printing resolution comes at the price of having a limited printing area. [21]
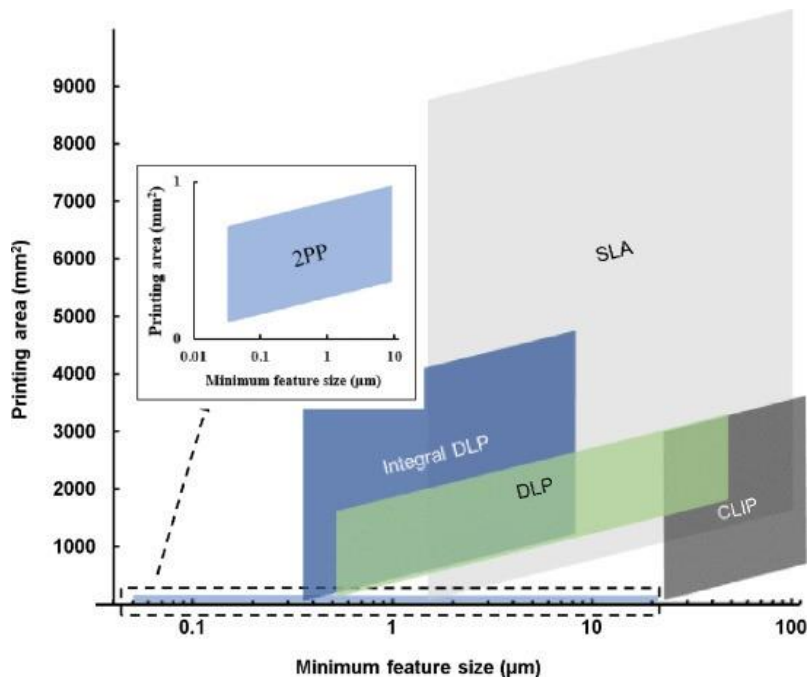

Figure 1.13: Plot reporting the adverse relation between the feature size and the printing area for vat photopolymerization

1.3 DLP method and types of photopolymerization

In this paragraph a further analysis of DLP is carried out, to explain in a more detailed way the process.

Digital Light Processing (DLP) is a 3D printing technology developed by Larry Hornbeck at Texas Instruments in 1987. Unlike Stereolithography (SLA), which uses a laser beam to trace and cure resin, DLP projects a complete digital image onto the resin vat using a digital micromirror device (DMD). This device consists of numerous tiny mirrors arranged in a matrix on a semiconductor chip. The image is first projected onto an optical diffuser, which scatters the light to microlenses that then focus it onto the build surface.

The resolution and build size in DLP printing depend on the number of micromirrors, their arrangement, and the lens system used. Higher resolution requires more micromirrors and sophisticated lens systems but traditionally comes at the cost of a smaller build area. To mitigate this, DLP printers can use a technique called stitching. This involves projecting the image in sequential steps, with the projector or vat moving to cover larger areas without sacrificing detail.

More recently, a third type of stereolithographic 3D printing has emerged, utilizing a liquid crystal display (LCD) screen as a mask to project the image. However, LCD screens only allow about 12.5% of light through compared to 88% for DMD devices. Additionally, LCD technology has larger pixels, higher failure rates in switching crystals, and a shorter lifespan, making them less reliable.

The main challenge in DLP printing is the trade-off between resolution and the size of the projected image due to the single-aperture projection system.

The resin, to be effective in this process, must possess two key characteristics: the ability to be cured by light, with a reaction activated by a photoinitiator, and an adequate fluidity. The most frequently used resins in DLP printing include acrylate, methacrylate, and epoxy resins, since they can be efficiently cured by light. However, beyond their light-curing properties, the viscosity of the resin plays a crucial role. A sufficient low viscosity is essential to allow the resin to flow freely within the vat, facilitating better coverage and reducing the likelihood of defects. Resins with low viscosity not only spread more easily and homogeneously in the VAT but also allow for better molecular diffusion. This increased diffusion enhances the reactivity during the photopolymerization process, thereby reducing the overall process time. Additionally, high viscosity can create several issues, starting from having inhomogeneities of the resin distribution in the VAT. Additionally, it can make difficult to detach the build platform during the lift-off process in bottom-up configurations, and it can also negatively affect the final resolution of the printed object. To manage the viscosity, thinners can be added to the resin. These thinners lower the viscosity, expanding the range of photopolymers that can be used in DLP printing.

In general, the suitable range of viscosity is around 0,2-10 Pa*s, with a developed shear rate during printing process of approximately 5-20 s^{-1}. [22]

Having said this, resins suitable for DLP technology generally undergo two types of photopolymerization: radical and cationic. In the next sections both will be explained in a detailed way.

Politecnico di Torino

1.3.1 Radical polymerization

Radical polymerization involves the creation of free radicals as reactive species from the decomposition of the photoinitiator, due to the latter's absorption of light.

The choice of photoinitiator depends on the specific wavelength of light used in the printing process. There are two types of radical photoinitiators: Norrish Type I and Norrish Type II.

Type I initiators generate radicals directly upon exposure to light, while Type II initiators produce radicals through a reaction with a co-initiator.

Among radical photopolymerizable resins, (meth)acrylate resins are the most used. These resins vary in their properties based on their functionality and molecular weight. Monofunctional acrylates usually have lower viscosities but higher processing time due to the single functional group, while multifunctional acrylates are more viscous, less flexible, and have shorter processing times due to the accelerated initiation phase of chain polymerization. However, (meth)acrylate resins face challenges such as volumetric shrinkage and oxygen inhibition. Shrinkage occurs because of the structural changes during polymerization, leading to potential distortions in the printed layers. Oxygen inhibition can be particularly problematic as it slows down the polymerization process and it can lead to uncured areas. [23]

Other radical systems include thiol-ene and thiol-yne resins. Thiol-ene systems react thiols with carbon-carbon double bonds, offering advantages such as reduced oxygen inhibition and lower shrinkage. However, they can be softer and have an unpleasant odor. Thiol-yne systems involve reactions between alkyl thiols and carbon-carbon triple bonds, creating highly cross-linked networks with increased modulus and glass transition temperature (Tg). Despite these benefits, their low conversion rates limit their use in DLP printing. [24]

1.3.2 Cationic polymerization

On the other hand, cationic polymerization uses cationic photoinitiators, usually salts, which decompose under UV light to produce reactive species. These species initiate a chain polymerization, forming strong acids (super acids) that continue the reaction. This process is less susceptible to oxygen inhibition, and the monomers used are generally non-toxic and less irritating compared to acrylates and methacrylates.

Epoxy resins are a common choice for cationic polymerization. They are characterized by low volumetric shrinkage during the ring-opening reaction, resulting in less stress within the printed parts. However, epoxy resins can be brittle. To address this, chain-transfer agents can be added to reduce cross-linking density, or different monomers can be mixed to modulate the photopolymerization speed and improve the mechanical properties of the final product. [25]

1.4 Overview on biobased photcurable resins

As highlighted in the introduction, the transition to a circular economy necessitates the replacement of fossil-based resins with bio-based alternatives. Over the past few decades, significant research has been dedicated to developing such alternatives, often utilizing vegetable oils intended for human and animal consumption. However, there are non-edible options that do not compete with food sources, including algae, lignin, cellulose, polysaccharides, and plant proteins. These materials are abundantly available and can serve as carbon precursors. Other carbon sources can be derived from waste and industrial by-products such as wood, wood pulp (from the paper industry), or starch. These sources typically require purification and chemical modification before they can be used as starting materials in polymerization processes. To minimize VOC emissions and waste, the purification and functionalization of these raw materials must adhere to environmental regulations. Furthermore, as already discussed in the introduction, UV polymerization is an energy-efficient process that operates at ambient or low temperatures and with short processing times, making it a "green" alternative to the standard high-temperature processes, making sense of the extensive research into the synthesis of biobased UV-curable resins. [26]

Talking about the already used feedstocks, vegetable and animal oils and fats are among the most utilized bio-based sources, particularly in the production of lubricants, coatings, and surfactants. These oils mainly consist of triglycerides, and their composition varies depending on the source species. While some vegetable oils, such as vernonia oil, contain functional groups like epoxide groups, others typically require chemical functionalization of triglycerides and fatty acids. Epoxidation is one of the most frequently employed methods of functionalization. The structure of the oils can then be further modified by introducing additional unsaturation, such as (meth)acrylate groups, which facilitate the photopolymerization process through radical photopolymerization.

In the field of bio-based coatings derived from vegetable oils, several studies have demonstrated the effectiveness of adding multifunctional thiols. These react with triglycerides due to the presence of multiple unsaturation, creating a polymeric network that makes the oil sensitive to UV curing without oxygen inhibiting the photopolymerization process. As previously mentioned, the (meth)acrylation of vegetable oils is a common method for making them UV-reactive, and it is used with various vegetable oils such as linseed, soybean, and rapeseed oils. The standard method of (meth)acrylation involves the use of an epoxidized oil and (meth)acrylic acid, which introduces new groups that simplify and expedite the photopolymerization process by enabling a radical mechanism.

Epoxidized oils, another category, are predominantly used in ink and adhesive manufacturing. Epoxidized soybean oil (ESO) is particularly popular, as its photopolymerization can occur in the presence of numerous photoinitiators. In its acrylate epoxidized form (AESO), it has been used as a feedstock for 3D printing using SLA and DLP methods. Vernonia oil is another widely used vegetable oil, with films made from it displaying high flexibility and impact resistance. [27]

Another area of interest is the synthesis of acrylate polyglycerol monomers, which are derived from natural triglycerides found in vegetable oils, such as palm oil, and animal fats.

Triglycerides, which are the main components of vegetable oils and animal fats, are first broken down into glycerol and fatty acids through processes known as saponification or, as alternative, hydrolysis.

Saponification process involves heating triglycerides in the presence of a strong base, such as sodium hydroxide (NaOH) or potassium hydroxide (KOH). The reaction produces glycerol and soap (the sodium or potassium salts of fatty acids), as visible from Figure 1.14 [28].
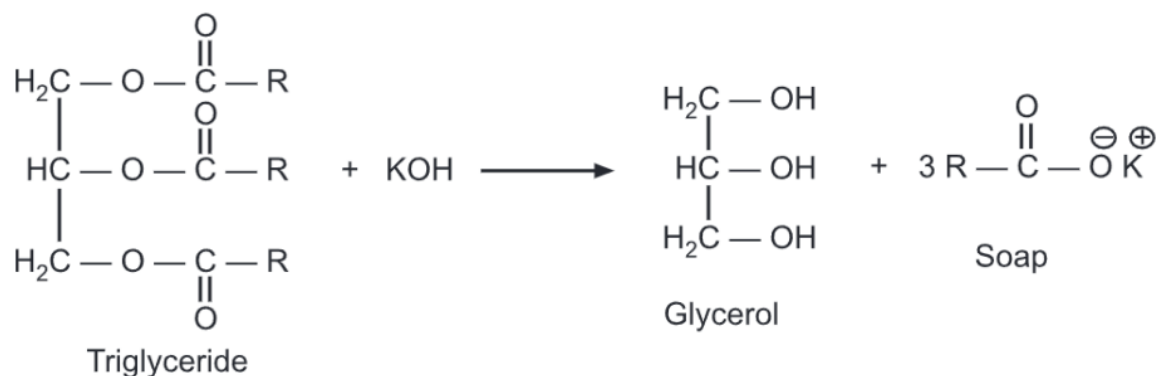

Figure 1.14: Scheme of saponification process

Alternatively, triglycerides can be hydrolyzed with water under high temperature and pressure, sometimes using a catalyst such as an enzyme (lipase), to yield glycerol and free fatty acids, as reported in Figure 1.15 [28].
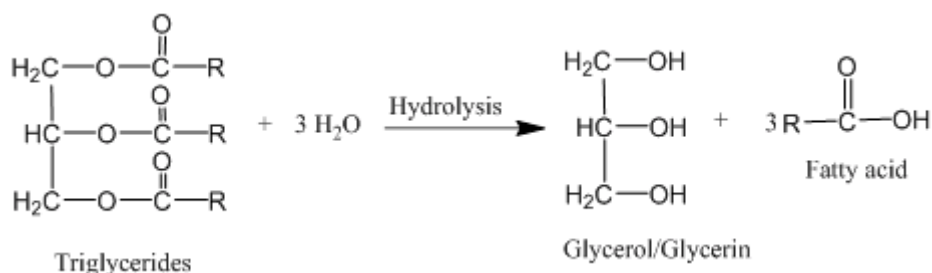

Figure 1.15: Refiguration of hydrolysis process

The glycerol obtained from the first step is then polymerized to form polyglycerol. This process typically involves the condensation of glycerol molecules under controlled conditions. Glycerol molecules are heated, usually in the presence of an acid or base catalyst, to form polyglycerol. The reaction involves the removal of water molecules, leading to the formation of ether bonds between glycerol units. The degree of polymerization can be controlled by adjusting the reaction conditions (temperature, time, catalyst concentration) to obtain polyglycerol with the desired molecular weight.

All the possible glycerol-based monomers obtainable from glycerol are reported in Figure 1.16. [29]
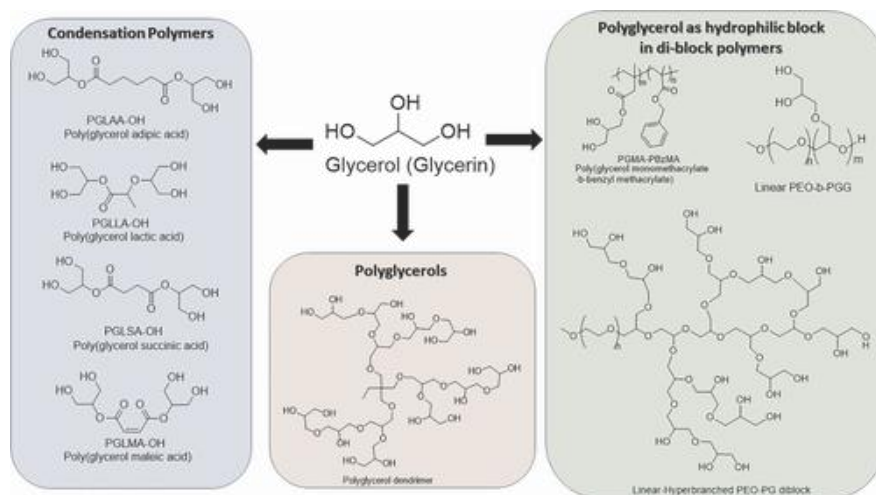
Figure 1.16: Possible ways to produce polyglycerol and glycerol-based monomers

The final step involves esterifying the hydroxyl groups of the polyglycerol with acrylic acid or its derivatives (like acryloyl chloride, methacrylic acid) to form acrylate polyglycerol monomers.

Polyglycerol reacts with acrylic acid in the presence of a catalyst (e.g., a strong acid like sulfuric acid or a Lewis acid) to produce acrylate ester groups on the polyglycerol backbone. The reaction may also require a dehydrating agent to remove the water formed during the esterification process, driving the reaction to completion. Sometimes, acryloyl chloride or methacryloyl chloride is used instead of acrylic acid to improve the efficiency of the esterification process. In this case, the reaction produces acrylate polyglycerol monomers and hydrochloric acid (HCl) as a byproduct.

This process results in multifunctional UV curable monomers that can be used in a variety of polymerization reactions to create materials with desirable properties for industrial, biomedical, and environmental applications. [30]

Furthermore, polysaccharides, such as starch and cellulose, are also significant sources of bio-based materials. These can be converted into monosaccharides and other simpler molecules, such as unsaturated carboxylic acids and furan derivatives, through enzymatic and chemical processes. Polysaccharides are among the most abundant natural polymers, extracted from a wide range of sources, including plants, animals, fungi, microorganisms, and marine organisms. At room temperature, they typically exist as fibers, pellets, or gels. The most common applications for these materials are in the biomedical sector, where their high biocompatibility makes them ideal for tissue engineering and drug delivery. However, they can also be used as light-curing materials after functionalization with acrylate groups. Polysaccharide based light curable materials are known as hydrogels, which are three dimensional hydrophilic polymers capable of absorbing large amounts of water. Various polysaccharides, including cellulose, starch, chitosan, alginate, and dextran, have been used to create hydrogels. Some studies have shown that bio-based hydrogels can be used for water purification, particularly in removing waste. Additionally, γ-cyclodextrin, a acrylate-methacrylate starch derivative, has been used as a multifunctional macromer to generate highly crosslinked structures through VAT polymerization 3D printing techniques. [31]

Proteins can also be used to create light-curing biopolymers through the process of adding methacrylate groups to amine groups, thereby enabling the photopolymerization of hydrogels. An example of a protein used in this context is silk fibroin, which can be derived from silkworms and is utilized in the biomedical field for producing dressings and vascular prostheses. Recent studies have indicated the potential for creating DLP printing inks through the methacrylation of silk fibroin. [32]

1.5 Scope of the study

Considering all the aspects reported in the previous sections, this thesis focuses on the use of environmentally affordable bio-derived acrylate polyglycerol monomers as a material for 3D printing, specifically aimed at creating electrically conductive components. To achieve this, liquid monomers were combined with varying types and amounts of conductive fillers.

To be precise, the 3D printing process employed was Digital Light Processing (DLP) using the bottom-up approach, a technique that, as already mentioned, uses UV radiation to cross-link the liquid resin layer by layer.

After formulating the mixtures with different filler types and concentrations, the liquid formulations were analyzed for their reactivity, degree of conversion, and rheological properties. Rheology tests were particularly crucial in identifying formulations with viscosities suitable for the printing process. Additionally, mechanical and thermo-mechanical characterizations were conducted on the 3D-printed samples to evaluate the properties of the cross-linked resin.

As introduced, the primary objective was to produce 3D-printed objects with a certain grade of electrical performance. To assess this, the electrical conductivity and Joule effect of bulk samples with various geometries were examined, with the testing conducted at the University of Madrid.

Politecnico di Torino

2 Materials and Methods

2.1 Materials

All the formulations were made using as polymeric matrix polyglycerol-based acrylic monomer, SYntech SA Serie SA-TE 12, procured from Sakamoto Yakuhin Kogyo Co., Ltd. (Osaka, Japan)., with a molecular weight of 1200 g/mol. The general chemical structure for SA-TE 12 monomer is represented in Figure 2.1. [33]
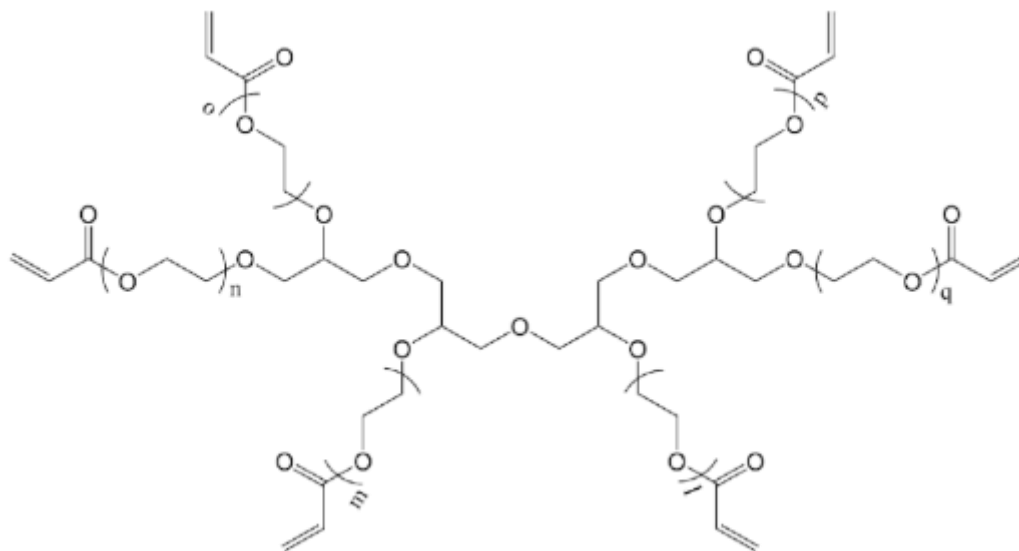

Figure 2.1: Chemical structure of SA-TE 12 monomer

The photoinitiator used was diphenyl(2,4,6-trimethylbenzoyl) phosphine oxide, purchased by Sigma Aldrich (Milan, Italy) under the trade name of Irgacure 819. Its chemical structure is reported in Figure 2.2. [34]
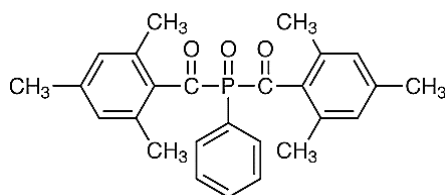

Figure 2.2: Chemical structure of diphenyl(2,4,6-trimethylbenzoyl) phosphine oxide (Irgacure 819), a radical photinitiator

Additionally, different types of fillers were introduced in different amounts. In particular, fillers were chosen in base of their conductivity, as higher as possible. The selected fillers are nichel (Ni), copper (Cu) and silver (Ag) under powder form and recycled carbon fibers (RCF), with a length of the fibers of 2 mm. All the metallic fillers were provided by Sigma-Aldrich and they have different granulometries: 5-8 µm for silver powder, 10-25 µm for copper powder and 3-7 µm for nichel. The RCF were supplied from the University of Madrid and recovered from dismissed composites.

2.2 Formulation preparation

A total of 15 formulations were investigated, each with different conductive filler content. Table 2.1 reports the studied formulations.

Table 2.1: List of formulations analyzed

Amount	Type
0 phr	SA-TE 12 pristine
5 phr	RCF
10 phr	RCF
25 phr	Ag, Ni, Cu
50 phr	Ag, Ni, Cu
75 phr	Ag, Ni, Cu
100 phr	Ag, Ni, Cu

In each formulation, 1 phr of radical photoinitiator was added. All formulations were placed in a sonication bath for about 10 minutes at 60°C in order to properly dissolve and homogenize the photoinitiator in fine powder form. Afterwards, THINKYMIXER ARE-250 planetary mixer was used to properly homogeneously distribute fillers in the monomer and degase the formulations. The program selected is the following: 1 min mixing and then 1 min degassing at 1600 rpm, 1 min mixing and then 1 min degassing at 1800 rpm, and finally 2 min mixing at 2000 rpm.

2.3 3D-printing via DLP technology

During the 3D printing phase for the obtainment of the samples, the Phrozen Sonic Mighty 4K printer was used. The printer itself is made by Phrozen but was modified by Sharebot, having created an aluminium reducer for the VAT and a suitable reduced build surface. It is a DLP-type printer with a digital mask, exploiting LED light source emitter with a wavelength of 405 nm. The resolution in the xy plane is 52 µm while in the z plane it is in the range of 10-300 µm. The growth platform used has a surface area of 50x50 mm^2 as usable surface for printing, and the maximum height of printable objects is 22 mm. As already mentioned, the VAT used is not commercially available and it was designed by Sharebot. The technical boards of the aluminum reducer and of the building platform provided by Sharebot are visible in Figure 2.3 and Figure 2.4, respectively.
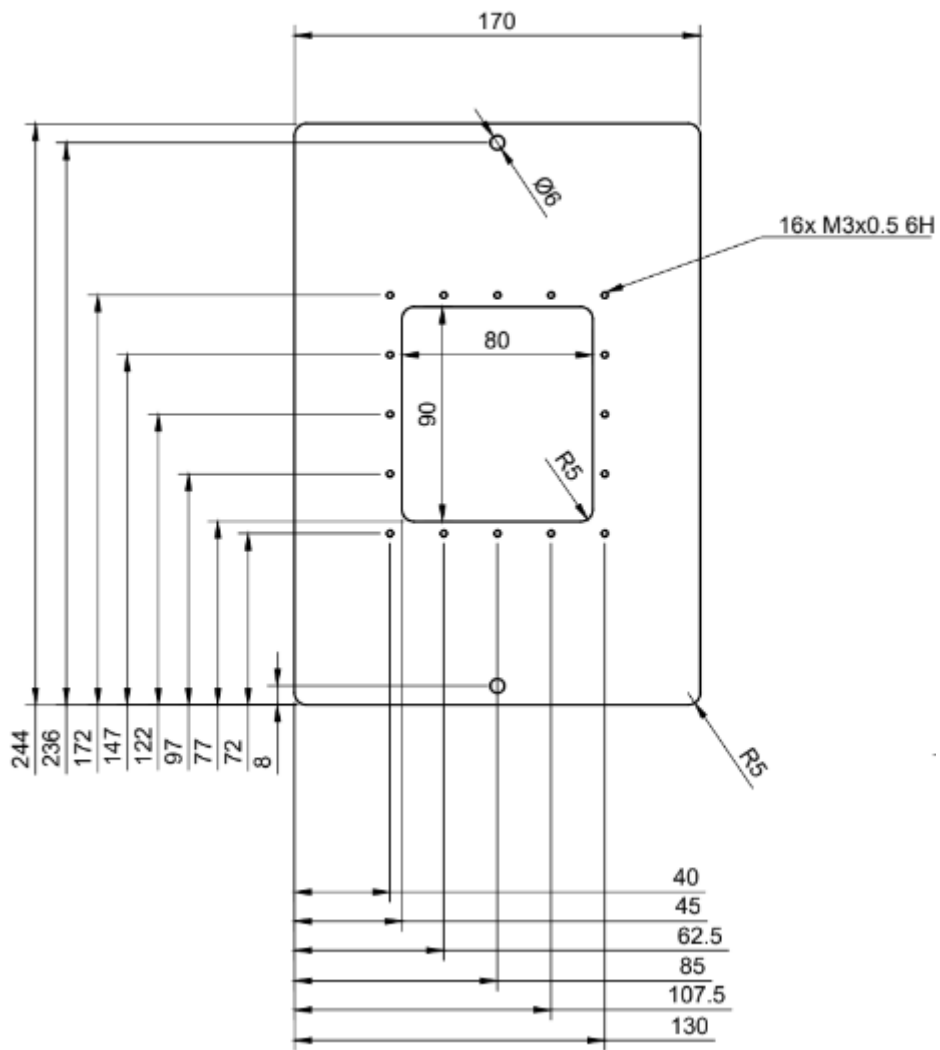
Politecnico di Torino

Figure 2.3: technical board of the vat reducer designed by Sharebot
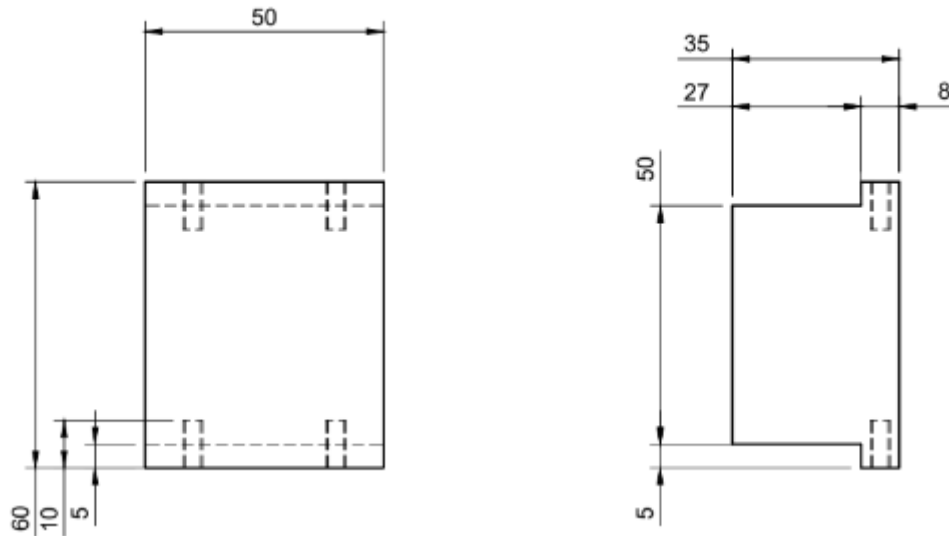
Figure 2.4: technical board of the adopted building platform designed by Sharebot

Printing parameters, such as the irradiation time of each layer, the intensity of the light, the thickness of each layer and the waiting time between irradiations, can be varied using the printer-compatible software, called Chitubox basic. These parameters were varied according to the type of formulation used, basically considering the amount in phr and the type of filler present, as reported in paragraph 3.2

In particular, the exposure time of the initial layers is separated from the exposure time of a generic layer. To allow adhesion between two dissimilar interfaces, that of the metal platform and the composite one of the objects under construction, the exposure time of the first 2 layers is significantly longer than that of the subsequent layers. Generically the higher the viscosity and the UV absorption power of the filler present the higher the exposure time necessary to properly cure.

In addition, it was possible to adjust the delay with which the UV lamp is switched on after each irradiation phase, giving the resin time to evenly fill the volume of the building. The higher the formulation viscosity the higher the delay necessary to permit the proper spread of the resin before the next irradiation step.

Other parameters remained fixed for each of the formulations, particularly the ones reported in Table 2.2.

Table 2.2: Constant printing parameters

Layer height [µm]	50
Bottom layer count	2
Lift distance [mm]	8
Lift speed [mm/min]	60
Retract speed [mm/min]	150

The printed samples are for DMTA, tensile and electrical behavior analysis. Specimens measuring 18x8x1 mm^3 were made for the DMTA. For the tensile test, dog-bone shaped specimens were produced using ISO 527A-5B standard, with a thickness of 1 mm [35]. In addition, complex geometries and proofs of concept, such as gyroids of 10 mm^3, were obtained to demonstrate the printability of formulations.

After printing, each specimen was immersed in isopropanol and placed in a sonication bath for 5 minutes to remove any uncured resin residue. Finally, the test specimens were placed inside a UV lamp provided by Phrozen to complete the photo cross-linking, performing the post-curing phase for approximately 15 min.

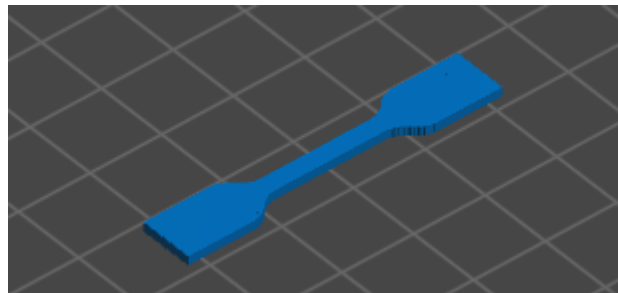The 3D CAD models of each of the printed samples are reported from Figure 2.5 to 2.9.

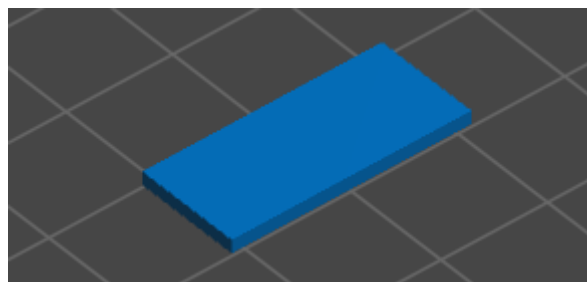*Figure 2.5: CAD model of ISO 527A-5B sample used for tensile tests*

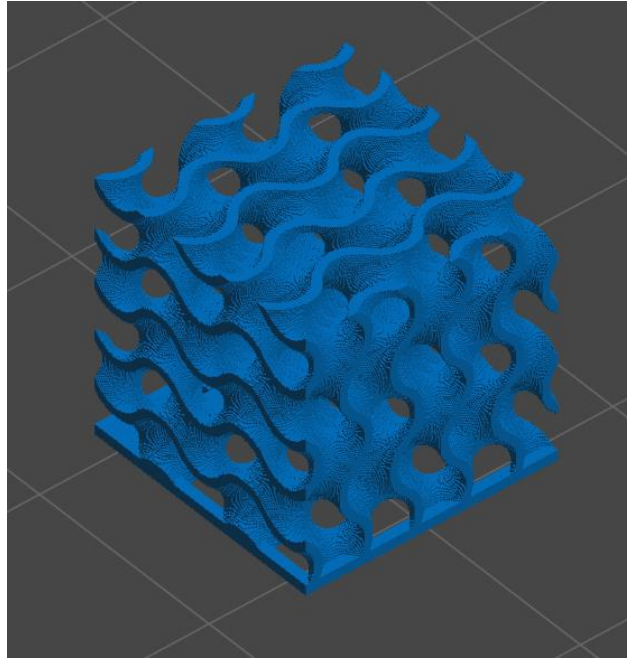*Figure 2.6: CAD model of sample used for DMTA*

Politecnico di Torino
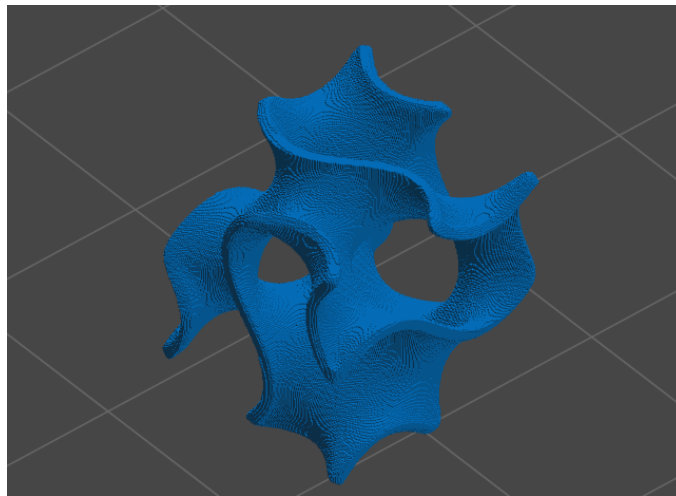
Figure 2.7: CAD model of a standard gyroid 10x10x10 mm^3

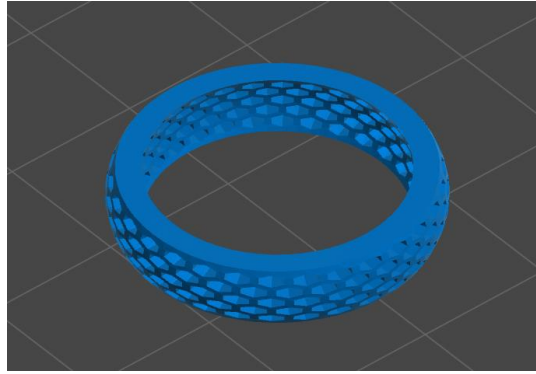*Figure 2.8: CAD model of a chunk gyroid 10x10x10 mm^3*

Figure 2.9: CAD model of a honeycomb ring for thermotherapy

2.4 Preliminary Characterizations of liquid monomers and formulations

To characterise the liquid formulations, the following tests were carried out:

1. Fourier Transformed Infrared spectroscopy (FT-IR), conducted to assess the degree of conversion after different UV exposure time for each formulation,
2. Differential scanning photo calorimetry (photo-DSC), to measure the speed of the chain-growth kinetic and heat released by the photopolymerisation process,
3. Rheology, a viscosity analysis to assess which formulations are suitable for printing.

2.4.1 FT-IR spectroscopy

FT-IR is based on the interaction of electromagnetic radiation, in the infrared range, with molecules of the sample. When the infrared photon is absorbed, the energy released by the radiation is converted into vibrational energy of the molecules, in particular each type of chemical bond has its characteristic vibrational mode. In this way, information on the chemical structure of the material can be obtained from the IR absorption spectrum of the sample analyzed. In fact, each chemical bond has absorption peaks in specific wave number ranges, for example the carbon-carbon double bond characteristic of acrylates has absorption peaks between 1680-1580 cm^{-1}. The spectra usually show the wave number [cm^{-1}] on the x-axis and the absorbance [%] on the y-axis.

In this thesis work, IR spectroscopy was used to check the conversion of the resin after exposure to UV light, after the photo-crosslinking process. In particular, since the used monomer have acrylate group, a lowering of the peak characteristic of acrylates, following UV exposure, was noted. The conversion was calculated using the equation below (1):

$$Conversion \% = \frac{(\frac{A_{functional}}{A_{reference}})_{t=0} - (\frac{A_{functional}}{A_{reference}})_{t}}{(\frac{A_{functional}}{A_{reference}})_{t=0}} \cdot 100$$

(1)

Where $A_{functional}$ is the peak area of the functional group under investigation during the test, specifically the acrylate group, and $A_{reference}$ is the area of the peak used as a reference, the carbonyl one in this case. With t=0 and t, the pre- and post-UV irradiation times are indicated, respectively.

The Thermo Scientific™ Nicolet™ iS50 FTIR spectrometer and Omnic™Spectra software were used to conduct this analysis, and Hamamatsu LC8 lamp was adopted for conducting the photo-crosslinking. The formulations were deposited on a silicon substrate with a spreader bar, in the form of films approximately 12 μm thick. Subsequently, the IR spectrum of the test sample was recorded prior to UV exposure (pre-curing, t=0 s). After that, each film was irradiated with the UV lamp for 10 s, 20 s, 30 s, 60 s, 120 s and 180 s at a distance of 5 cm from the light source and at 1% intensity, with a resulting irradiation energy of about 10 mW/cm^2. After each irradiation, the IR spectrum of the sample was again recorded by noting the irradiation time t [s]. In a second period the conversion percentage of the samples is followed and reported as a function of the exposure time, from 0 to 180 s.

2.4.2 PhotoDSC

The photo-DSC analysis was performed with the Mettler TOLEDO DSC-1 instrument and a Hamamatsu LC8 type mercury lamp, with a wavelength of 365 nm. For this test, the lamp was used at 10% of the total intensity, with a resulting irradiation energy of 35 mW/cm^2. For each test, 5-10 mg of liquid resin was placed inside an aluminium crucible with a volume of 40 μL, while an empty crucible was used as a reference. The tests were carried out at a temperature of 25°C, in a nitrogen atmosphere with a flow rate of 40 ml/min, and three samples were analysed for each formulation. The cycle to which the sample was subjected during the test consisted of two steps, each characterised by 2 minutes of lamp off to homogenize the temperature and the atmosphere of the chamber, followed by 1 minute of UV irradiation. The second step was performed to obtain the baseline. This second curve obtained was subtracted from that of the first step, in order to obtain a curve related only to the light-curing of the sample. In this way, graphs of the enthalpy [W/g] as a function of time [s] were obtained. The height of the peak (h_{peak}) is proportional to the polymerisation rate, so the higher this value, the faster the polymerisation kinetics.

2.4.3 Rheology

Rheological characterizations were performed using the Anton Paar MCR302 parallel plate rheometer. Rheology was carried out to generally assess the viscosity of the formulations prepared, in order to determine which of them were the more suitable for the bottom-up DLP printing process.

Two 25 mm diameter plates were used for this analysis and a 1 mm gap was left between them. Viscosity values were recorded in a shear rate range between 1 and 1000 s^{-1}. Measurements were taken at a constant frequency of 1 Hz and a constant temperature of 25°C, viscosity [Pa*s] is reported as a function of the shear rate [s^{-1}].

Politecnico di Torino

2.5 Characterizations on the printed samples

Regarding cross-linked samples, made using a bottom-up DLP printing method, they were characterized through the following analyses:

1. Thermal mechanical dynamo analysis (DMTA) was performed to assess the thermomechanical behaviour of the resins, with the Tg trend as a function of the amount of reactive diluent inserted,
2. Tensile test, an analysis of the tensile behaviour of the test specimens,
3. Field Emission Scanning Electron Microscopy (FESEM) was used to analyze the fracture surface of the tensile test specimens,
4. Electrical conductivity test: determination of the electrical parameters of the material,
5. Thermal imaging: analysis of the Joule effect of test specimens during current flow.

2.5.1 DMTA

The Dynamic Mechanical Thermal Analysis (DMTA) was conducted using the Triton Technology instrument exclusively under tension mode with the application of a uniaxial stress, with a frequency of 1 Hz. Tests were conducted using liquid nitrogen to cool the chamber to approximately -30 °C and were terminated when the rubbery plateau was reached, with a heating rate of 3 °C/min. It is an analysis that allows the viscoelastic properties of polymers to be measured. In fact, when a cyclic stress is applied to the sample, the deformation of the polymer material will have an elastic deformation component, represented by the conservative modulus E', and a viscous deformation, represented by the dissipative modulus E". The relationship between these two quantities is called the damping factor, indicated by tan (δ). One of the curves obtained from the measurement is precisely the value of tan (δ) as a function of temperature [°C], given by the machine software as a ready to read output. At the maximum value of tan(δ), the peak of the curve, it is possible to identify the value of the glass transition temperature.

2.5.2 Tensile test

Tensile tests were used to investigate the mechanical properties of the crosslinked formulations. They were carried out on the specimens described in Section 2.3 and 3 specimens per formulation were tested. The MTS QTestTM/10 Elite instrument from the MTS System Corporation and TestWorks4 software were used for these tests. A 50 N cell was used as the load cell and tensile stress was applied at a rate of 5 mm/min. A stress-strain curve was obtained from each test, from which it was possible to derive the Young's modulus (E) value, calculated as the tangent of the curve in the linear zone, and also the maximum strain value. Each test ended with the sample breaking. The values of modulus and deformation at break are the result of the average of the 3 samples tested for each formulation.

2.5.3 FESEM

FESEM analysis of the broken sample from tensile tests were conducted on 50 phr Ag, Cu and Ni formulations and on 5 phr RCF formulation. More precisely, 3 photos were taken, with the TESCAN MIRA3, for each sample to indagate fillers dispersion and orientation inside the polymeric matrix. The analyzed surface was covered with a 10 nm thick platinum layer.

Politecnico di Torino

2.5.4 Electrical conductivity analysis and Joule effect evaluation

Conductivity and Joule effect analysis were performed on samples like those for DMTA, discussed on paragraph 2.3, for each formulation. The evaluation itself was conducted by Alberto Jiménez Suárez of Universidad Rey Juan Carlos Campus de Móstoles in Madrid, Spain.

The electrical conductivity tests were carried out by using a Keithley 2410 source-meter. The dimensions of the specimens were 18x8x1 mm3. Silver conductive paint was used in two 18x1 mm2 opposite faces of the specimen to minimize contact resistance. Here, the electrical resistance (R) was calculated from the voltage intensity (V-I) slope, considering Ohm's law, by sweeping the voltage from 0 to 3 V. Then, the electrical conductivity (σ) was calculated from Equation 2, where L is the distance between the electrodes, and A the cross-sectional area.

$$\sigma = L/(A \cdot R)$$

(2)

The Joule heating characterization was carried out by using a FLIR T530 thermal camera while applying voltage ranging from 1 to 15 V using the same source-meter equipment and specimens as in the electrical characterization tests. Here, the maximum and average temperatures, T_{max} and T_{av}, respectively, were recorded once the temperature was stable on time for each applied voltage. Furthermore, the homogeneity in Joule heating (H) was calculated from Equation 3.

$$H = 1 - (T_{max} - T_{av})/T_{av}$$

(3)

3 Results and discussions

This chapter reports and discusses the results for both liquid formulations and samples produced by the 3D printing process.

3.1 Analysis of liquid monomers and formulations

3.1.1 FT-IR spectroscopy

The liquid formulations were subjected to infrared spectroscopy, collecting the measurements after different exposure time: 0, 10, 20, 30, 60, 120 and 180 s of UV irradiation. Figure 3.1 shows, as an example, the spectra of SA-TE12 with 100 phr Ag. The spectrums of the other formulations are very similar to the reported one.
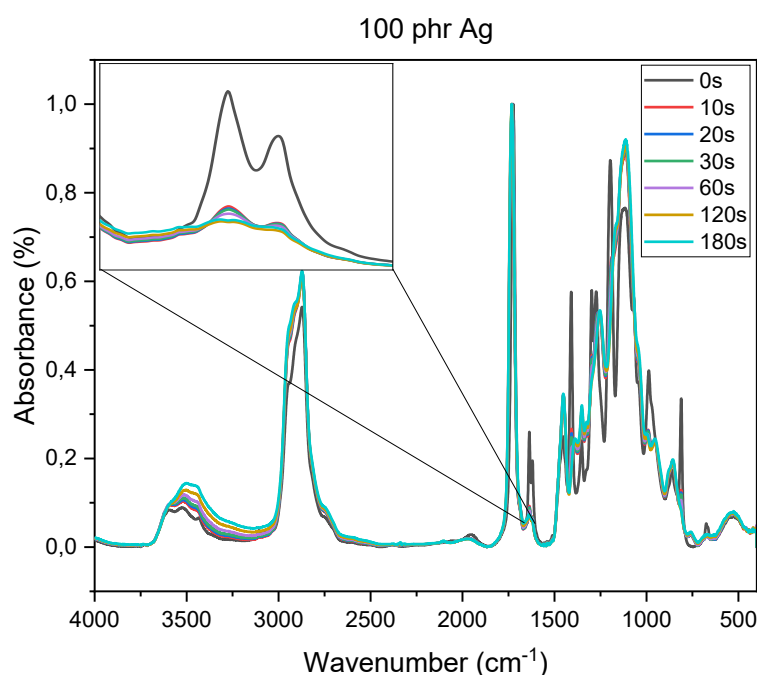

Figure 3.1: SA-TE12 with 100 phr silver powder absorbance FT-IR spectrum

To measure the conversion rate under UV irradiation of the formulations, the carbon-carbon double bond (C=C) peak, characteristic of the acrylate group, was monitored between 1680 and 1580 cm^{-1}, shown enlarged in the graphs. This peak was chosen because it is largely modified during the cross-linking process of these formulations. In fact, those carbon-carbon double bonds diminish by increasing the crosslinking grade, resulting in a lower peak characteristic of the acrylate group after UV irradiation.

On the other hand, the peak of the carboxylic bond (C=O), between 1780 and 1680 cm^{-1}, was chosen as the reference peak, since it practically remains unchanged during the cross-linking process.

Using equation (1) reported in section 2.4.1, the conversion percentage was calculated, choosing the area of the characteristic peak of the C=C bond as $A_{functional}$ and the area of the characteristic peak of the C=O bond as $A_{reference}$. This calculation was performed for all formulations. From Figure 3.2 to 3.5 the conversion curves as a function of irradiation time are reported for all the investigated

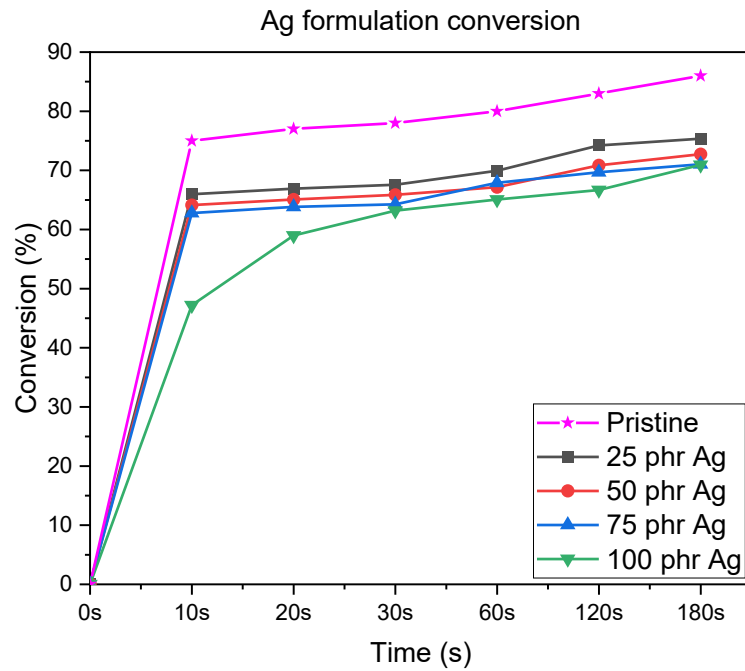formulations, while Table 3.1 shows the conversion values after 180 s of UV irradiation for each formulation.

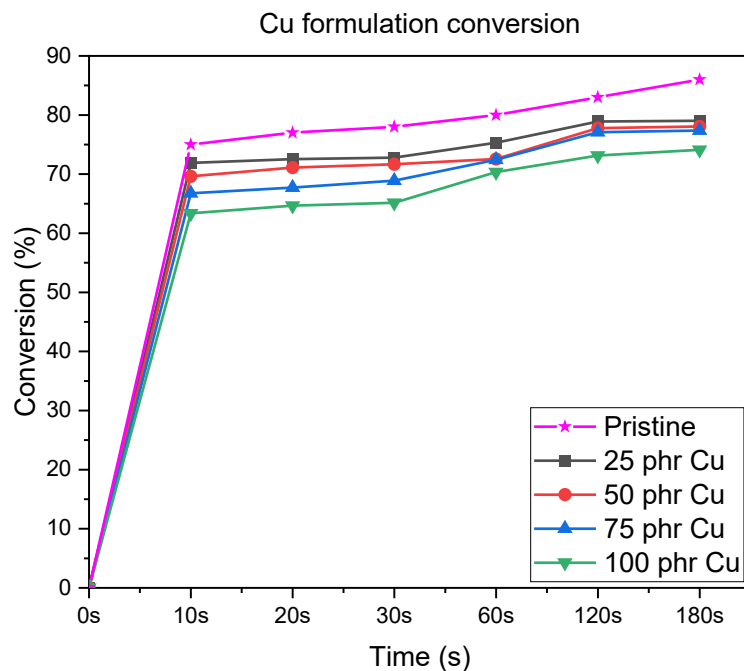*Figure 3.2: Conversion grade of SA-TE12 varying the content of silver powder*

Figure 3.3: Conversion grade of SA-TE12 varying the content of copper powder
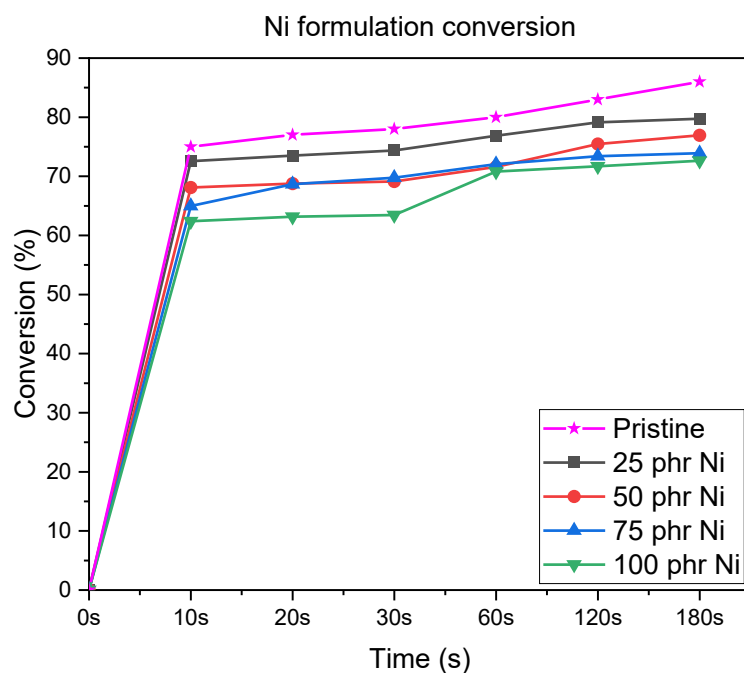

Figure 3.4: Conversion grade of SA-TE12 varying the content of nickel powder
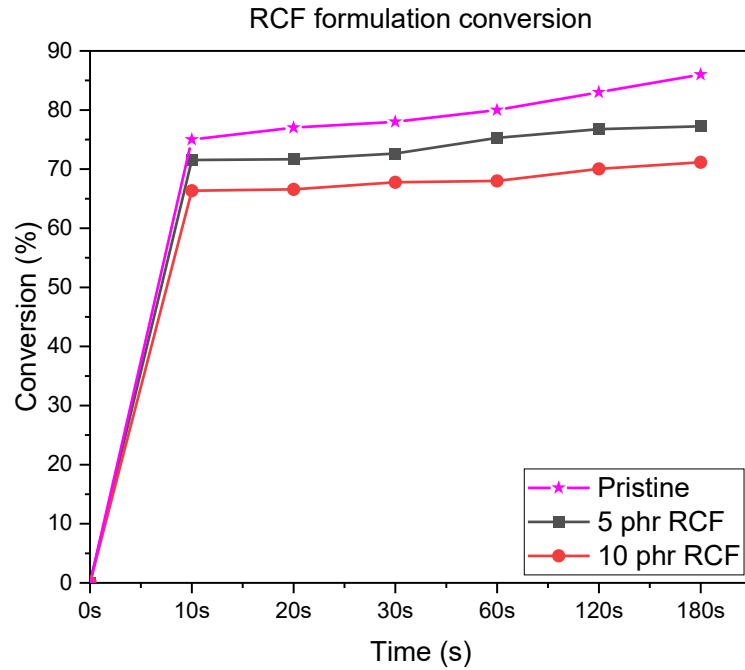
Figure 3.5: Conversion grade of SA-TE12 varying the content of recycled carbon fiber

Table 3.1: Conversion grade after 180s of UV irradiation for all the analyzed formulations

Formulation	Conversion at 180s [%]
SA-TE 12 Pristine	86
25 phr Ag	75
25 phr Cu	79
25 phr Ni	80
50 phr Ag	73
50 phr Cu	78
50 phr Ni	77
75 phr Ag	71
75 phr Cu	77
75 phr Ni	74
100 phr Ag	71
100 phr Cu	74
100 phr Ni	73
5 phr RCF	77
10 phr RCF	71

As can be seen from the above values, the conversion rate slightly decreases as the amount, expressed in phr, of filler increases in the photocurable formulation. This is mainly due to two factors. The first factor is the increase in viscosity of the formulation as the amount of filler increases. This

can hinder the movement of the carbon chains and thus the reaction between them and the photoinitiator, affecting photo cross-linking. The second aspect is related to the lower absorption of UV light by the photoinitiator, since an increase in the amount of filler correlates with a greater shielding and absorption effect by the latter. In particular, the table shows that the same phr content, but different fillers correspond to different UV absorptions. In particular, RCF appear to be the filler with the greatest absorbing and shielding power, as lower phr values (max. 10 phr) result in lower conversion values than those obtained with metal powder fillers but with significantly higher phr (25 to 100 phr).

3.1.2 PhotoDSC

The PhotoDSC analysis was conducted on 3 samples for each formulation to subsequently have a weighted average over a certain standard deviation of the values obtained.

The average of time-dependent specific heat flow curves of all formulations are shown, divided according to the fillers used, from Figure 3.6 to Figure 3.9.
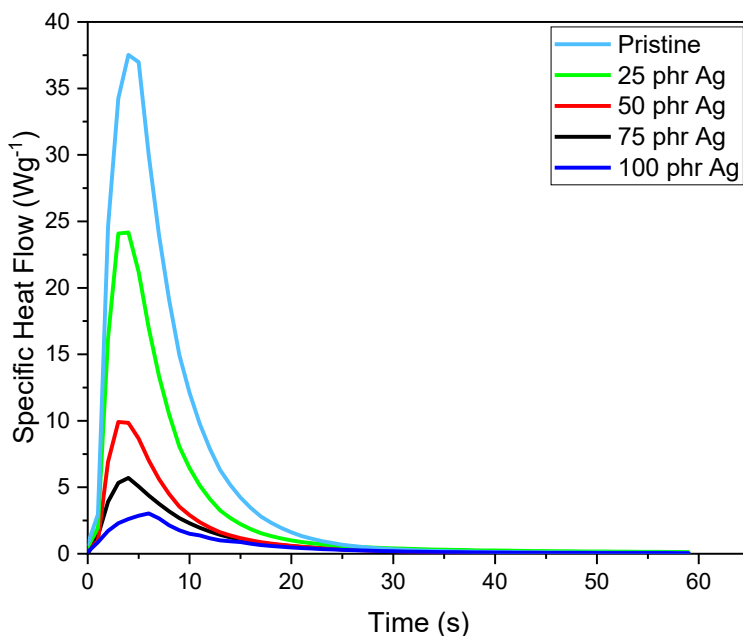

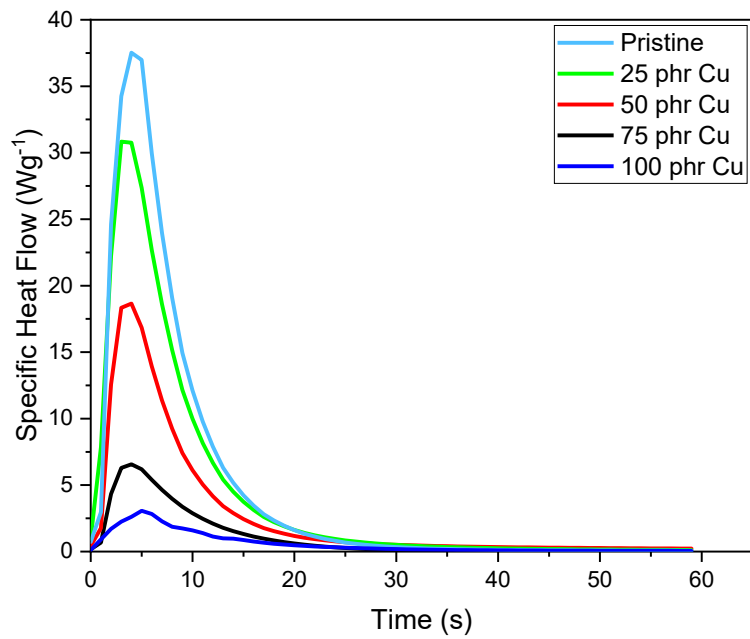*Figure 3.6: PhotoDSC plot of SA-TE12 varying the content of silver*

Figure 3.7: PhotoDSC plot of SA-TE12 varying the content of copper
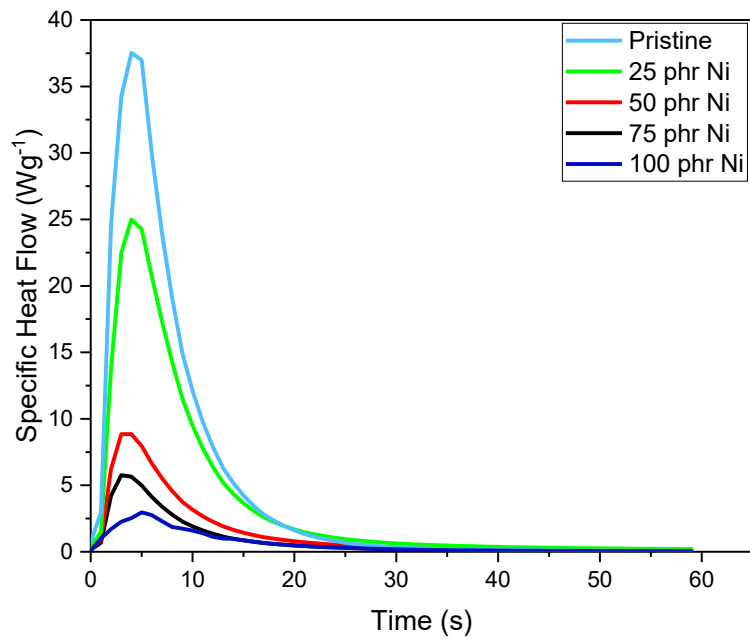

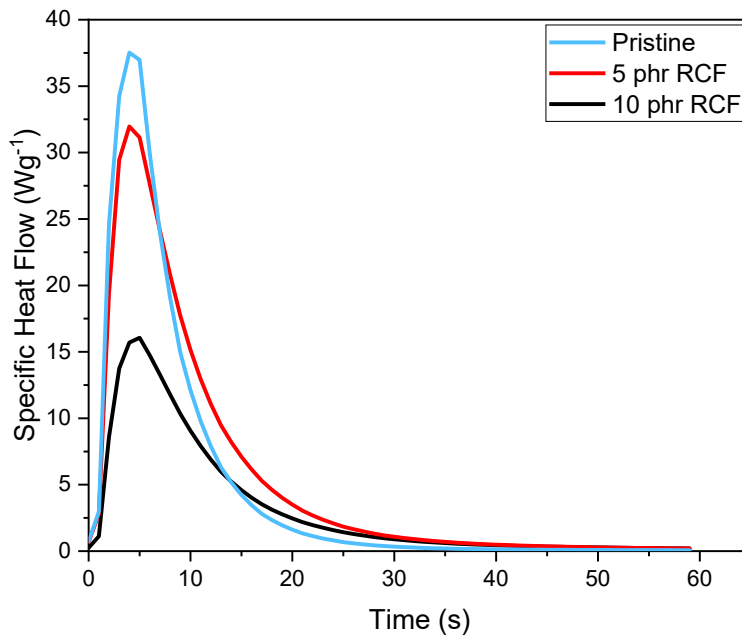*Figure 3.8: PhotoDSC plot of SA-TE12 varying the content of nickel*

Figure 3.9: PhotoDSC plot of SA-TE12 varying the content of recycled carbon fiber

Additionally, Table 3.2 shows the average values of h_{peak} (maximum value of the curve), t_{peak} (the time taken to reach the maximum of the curve) and the specific heat flow, calculated as the integral of the curve. As already anticipated, these values were calculated as the average of the values of the 3 samples analyzed for each formulation. The standard deviation was also calculated.

Table 3.2: average values of hpeak (maximum value of the curve), tpeak (the time taken to reach the maximum of the curve) and the specific heat flow characteristic of the studied formulations

Formulation	h_{peak} [W/g]	t_{peak} [s]	ΔH [J/g]
SA-TE12 Pristine	46 ± 5	2 ± 1	333 ± 44
25 phr Ag	25 ± 1	4 ± 1	212 ± 10
25 phr Cu	31 ± 1	3 ± 1	246 ± 23
25 phr Ni	24 ± 1	4 ± 1	207 ± 10
50 phr Ag	10 ± 1	4 ± 1	78 ± 11
50 phr Cu	18 ± 1	4 ± 1	145 ± 16
50 phr Ni	9 ± 1	4 ± 1	75 ± 15
75 phr Ag	6 ± 2	5 ± 2	52 ± 3
75 phr Cu	7 ± 1	5 ± 1	60 ± 9
75 phr Ni	6 ± 1	5 ± 1	47 ± 8
100 phr Ag	3 ± 1	5 ± 1	24 ± 3
100 phr Cu	3 ± 1	5 ± 1	21 ± 3
100 phr Ni	3 ± 1	5 ± 1	22 ± 3
5 phr RCF	32 ± 2	5 ± 1	303 ± 39
10 phr RCF	16 ± 1	5 ± 1	175 ± 12

Politecnico
di Torino

As visible from the graphs and values in the table, as the phr content of filler increases, the value of h_{peak} [W/g] and ΔH [J/g] decreases and t_{peak} [s] increases. Knowing that the value of h_{peak} is related to the polymerisation rate [], it is possible to state that an increase in the amount of filler leads to a decrease in the speed of the process. This is because the polymerisation rate depends on the concentration of the monomer and photoinitiator and is hindered by the presence of shielding or UV-absorbing elements such as metal powders and carbon fibres. Additionally, it may also be related to increasing viscosity as the filler content increases. In fact, as the formulation is more viscous, the chains have reduced mobility, thus decreasing the photopolymerization rate.

Concerning t_{peak} value, in accordance with all formulation types there is an increase in this parameter as the filler content increases, for the same reason as described above. As the formulation is more viscous by increasing the filler phr, the chains have reduced mobility, thus increasing the time required to reach the maximum curve.

Regarding enthalpy, its value diminishes as the amount of filler increases. Enthalpy is related to the energy of the photopolymerisation process, the opening energy of the double bonds. As the content of fillers increases, this energy decreases, presumably for the same reasons as described above, due to UV shielding and absorption effect of the filler mainly.

It can therefore be concluded that the photo-DSC measurements agree with the FT-IR measurements, except for the behavior of RCF formulations, which show a generally higher reactivity than expected when observing the degree of FT-IR conversion.

3.1.3 Rheology

Rheological measurements were conducted to study the viscosity and dynamic behavior of the prepared formulations. Figures from 3.10 to 3.27 show the viscosity curves as a function of the shear rate applied for both types of formulations. Additionally, the range of viscosity suitable for DLP 3D printing, going from 0,2 to 10 Pa*s, in a typical shear rate range present during the printing process, usually from 5 to 20 s^{-1}, is reported as a pale green area in all the plots.
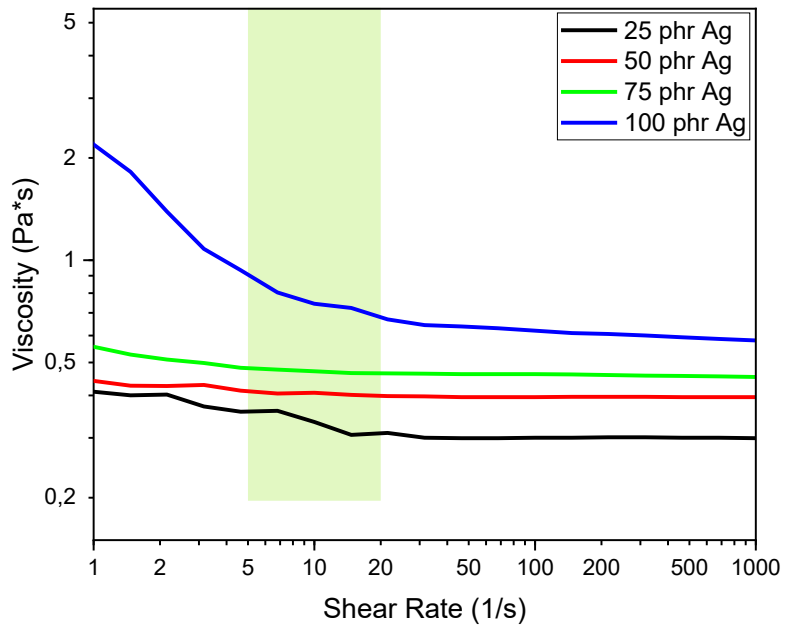
Politecnico
di Torino

Figure 3.10: Viscosity curves as a function of the shear rate of SA-TE12 varying the silver content
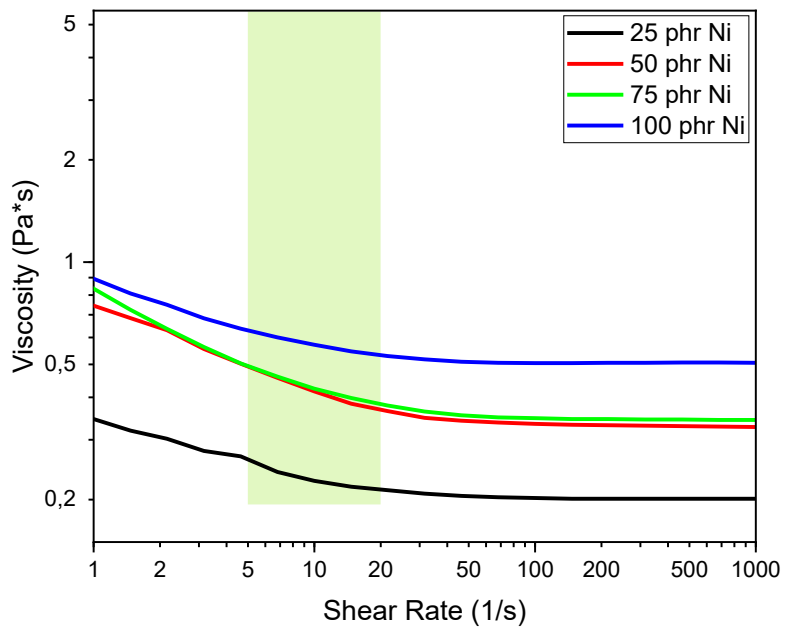

Figure 3.11: Viscosity curves as a function of the shear rate of SA-TE12 varying the nickel content
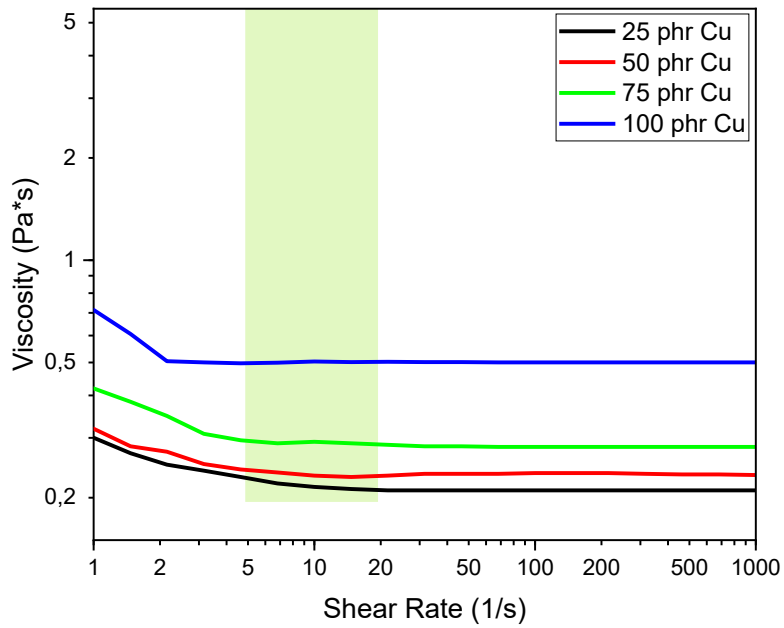
Figure 3.12: Viscosity curves as a function of the shear rate of SA-TE12 varying the copper content
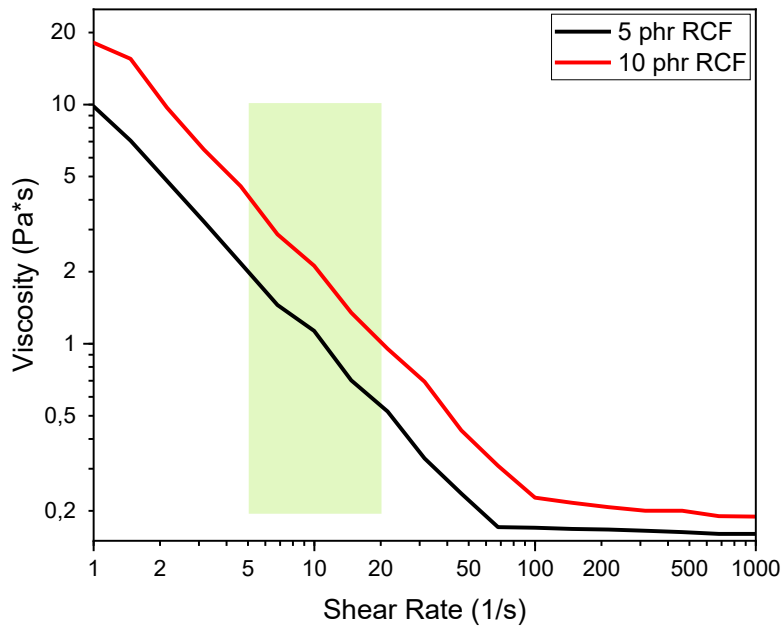

Figure 3.13: Viscosity curves as a function of the shear rate of SA-TE12 varying the recycled carbon fiber content

The rheological analyses were basically carried out to determine which formulations are suitable for the bottom-up DLP 3D printing process. As mentioned, in the literature, the viscosity values suitable for DLP printing are between 0.2 and 10 Pa-s, while the shear rate range characteristic of the process is between 5 and 20 s-1 [67]. From the images, it can be established that all the formulations treated turn out to be largely printable. In fact, it is possible to appreciate how, in the range of shear rates indicated the viscosity of all formulations turns out to be within the light green box, an index of printability.

In addition to the showed graphs, in Table 3.3 the value of viscosity, expressed in Pa*s, is reported for all the formulations at a shear rate of 5 s^{-1}.

It's noticeable how the general trend is that as the conductive filler content increases, viscosity increases in all formulations.

As one would have expected from the previous analyses, and confirming the reasons given, the formulations containing RCF turn out to be the most viscous, while remaining within the indicated limits of printability.

Table 3.3: Viscosity values at a shear rate of 5 s^{-1} of the studied formulations

Formulation	Viscosity [Pa*s] at 5 s^{-1}
25 phr Ag	0,36 ± 0,05
50 phr Ag	0,41 ± 0,07
75 phr Ag	0,58 ± 0,01
100 phr Ag	0,93 ± 0,02
25 phr Cu	0,23 ± 0,01
50 phr Cu	0,24 ± 0,02
75 phr Cu	0,29 ± 0,04
100 phr Cu	0,50 ± 0,1
25 phr Ni	0,27 ± 0,06
50 phr Ni	0,50 ± 0,01
75 phr Ni	0,51 ± 0,03
100 phr Ni	0,64 ± 0,05
5 phr RCF	2,2 ± 0,4
10 phr RCF	4,6 ± 0,9

Politecnico di Torino

3.2 Analysis conducted on printed samples

During the printing phase, the printing parameters shown in Table 3.4 were used, depending on the type of formulation and introduced filler.

Further constant, formulation-independent parameters are given in section 2.3.

Table 3.4: Printing parameters adopted as a function of the formulation type

Ag, Ni and Cu	Bottom exposure time	Exposure time	Light off delay
25 phr	200 s	5 s	10 s
50 phr	250 s	10 s	15 s
75 phr	280 s	10 s	20 s
100 phr	300 s	20 s	25 s
RCF			
5 phr	300 s	10 s	20 s
10 phr	400 s	25 s	30 s

As introduced in paragraph 2.3, it is noticeable that by increasing the amount of filler, or depending on the type of filler, all the parameters in the table above must be increased to enable a successful printing process. This is due to the higher viscosity of the formulation and the increase in UV shielding/absorption with increasing filler content. Additionally, it is appreciable the different behavior required for RCF due to their greater ability to increase the viscosity of the formulation.

With the formulations established printable from the rheological analyses, the samples, already introduced in section 2.3, were printed. In particular, samples were obtained through DLP printing for the analysis of mechanical properties by means of tensile tests, for the analysis of thermo-mechanical properties by means of DMTA, for the investigation of thermo-electrical properties and to investigate the feasibility of printing complex objects. Geometrically complex samples can be seen from Figure 3.14 to Figure 3.19.

In the following paragraphs, the results of analyses performed on samples made with DLP printing with the parameters discussed above.
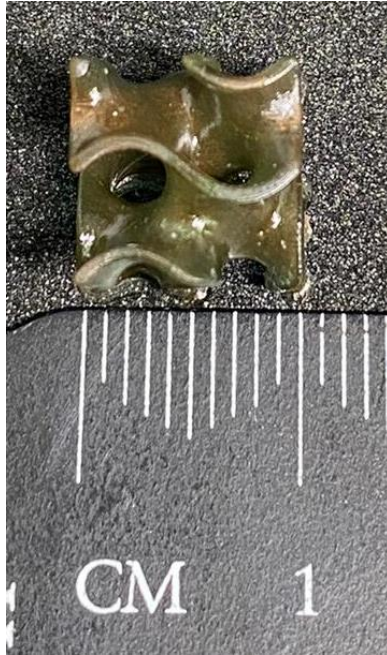
Politecnico
di Torino

Figure 3.14: Chunk gyroid printed using SA-TE12 with 75 phr Cu

Figure 3.15: Chunk gyroid printed using SA-TE12 with 75 phr Ag

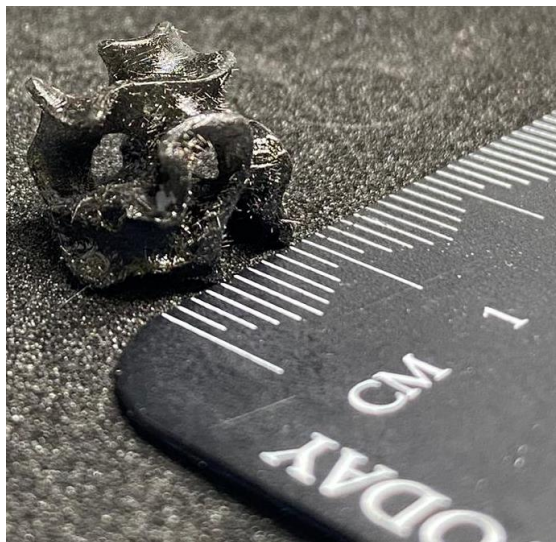*Figure 3.16: Chunk gyroid printed using SA-TE12 with 75 phr Ni*

Figure 3.17: Chunk gyroid printed using SA-TE12 with 5 phr RCF

Figure 3.18: Honeycomb ring printed using SA-TE12 with 100 phr Ag
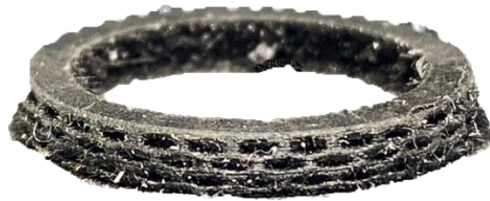

Figure 3.19: Honeycomb ring printed using SA-TE12 with 10 phr RCF

3.2.1 DMTA

The analysis was carried out on three samples of each formulation. Figures 3.20 to 3.23 show the curves of tan(δ) (TanDelta) and conservative modulus E' as a function of temperature for all the formulations treated.

Figure 3.20: TanDelta and E' curves as a function of temperature for Ag formulations

Figure 3.21: TanDelta and E' curves as a function of temperature for Cu formulations
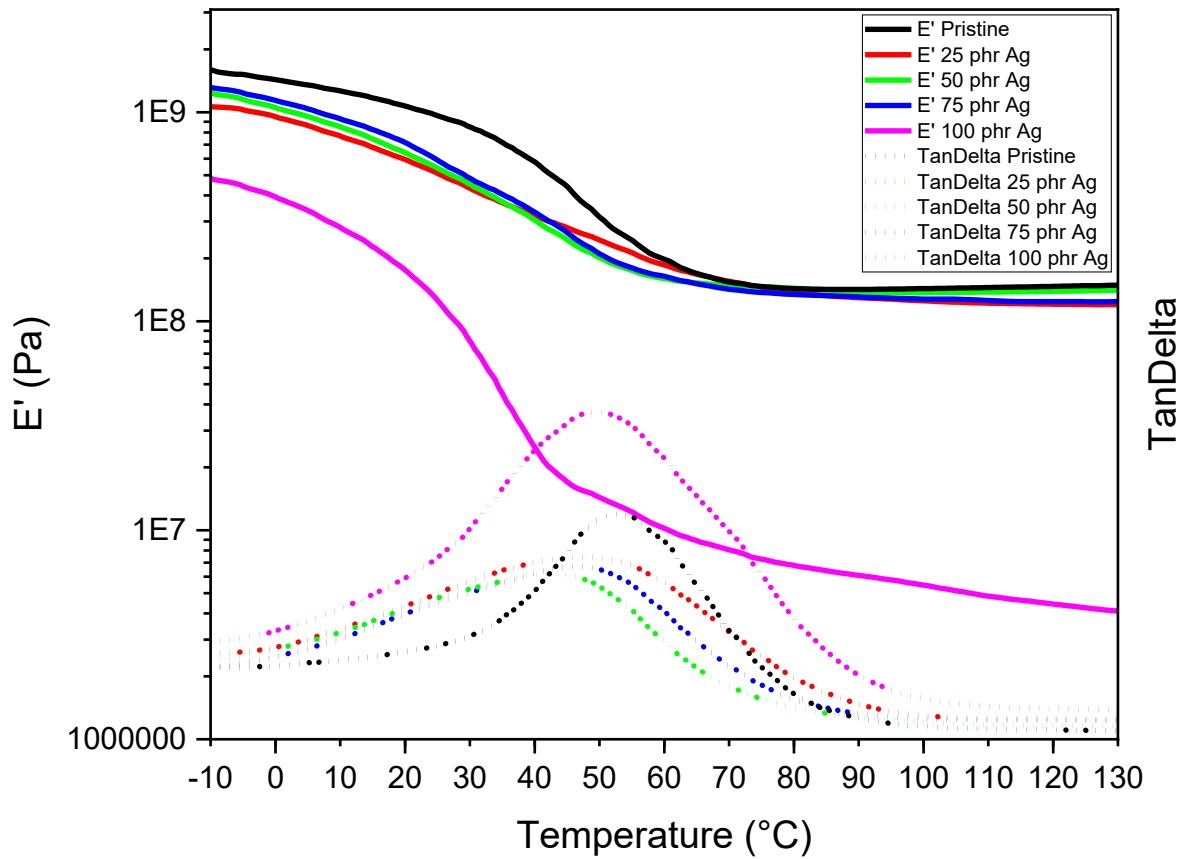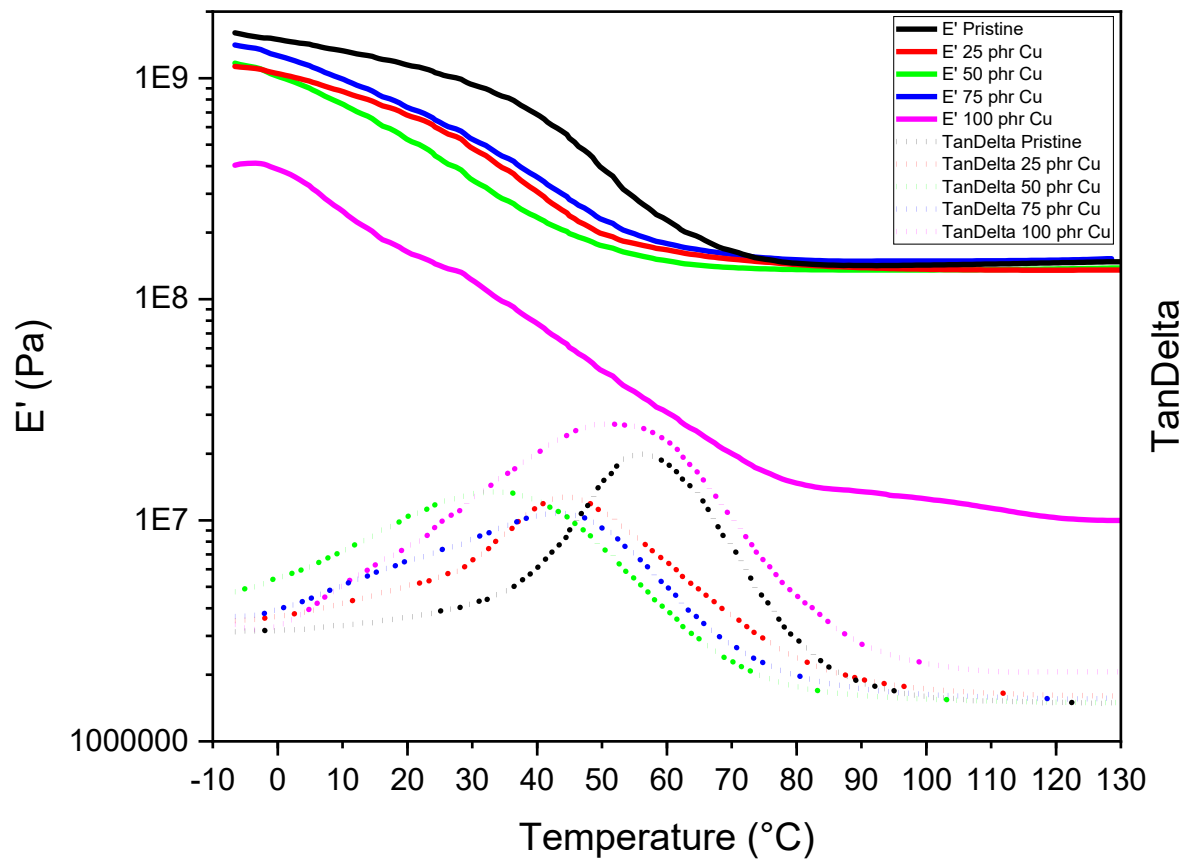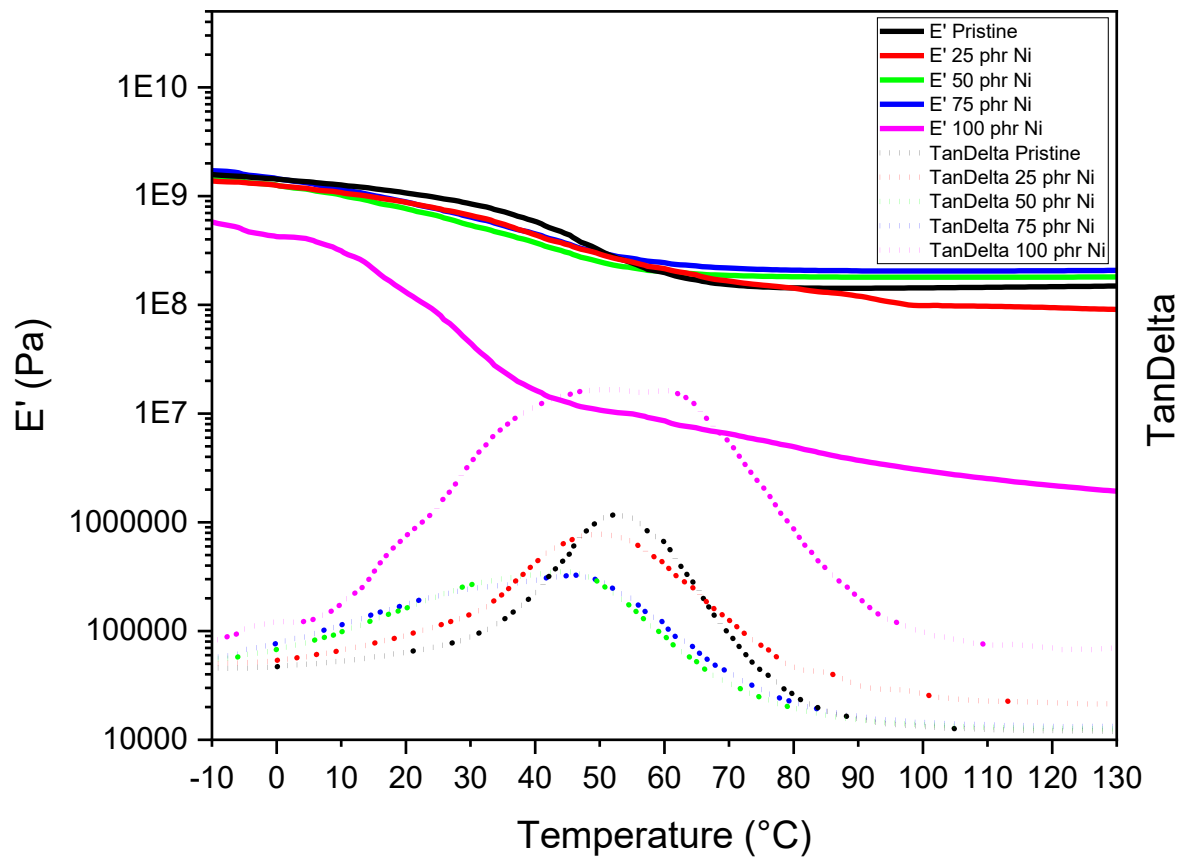
Figure 3.22: TanDelta and E' curves as a function of temperature for Ni formulations
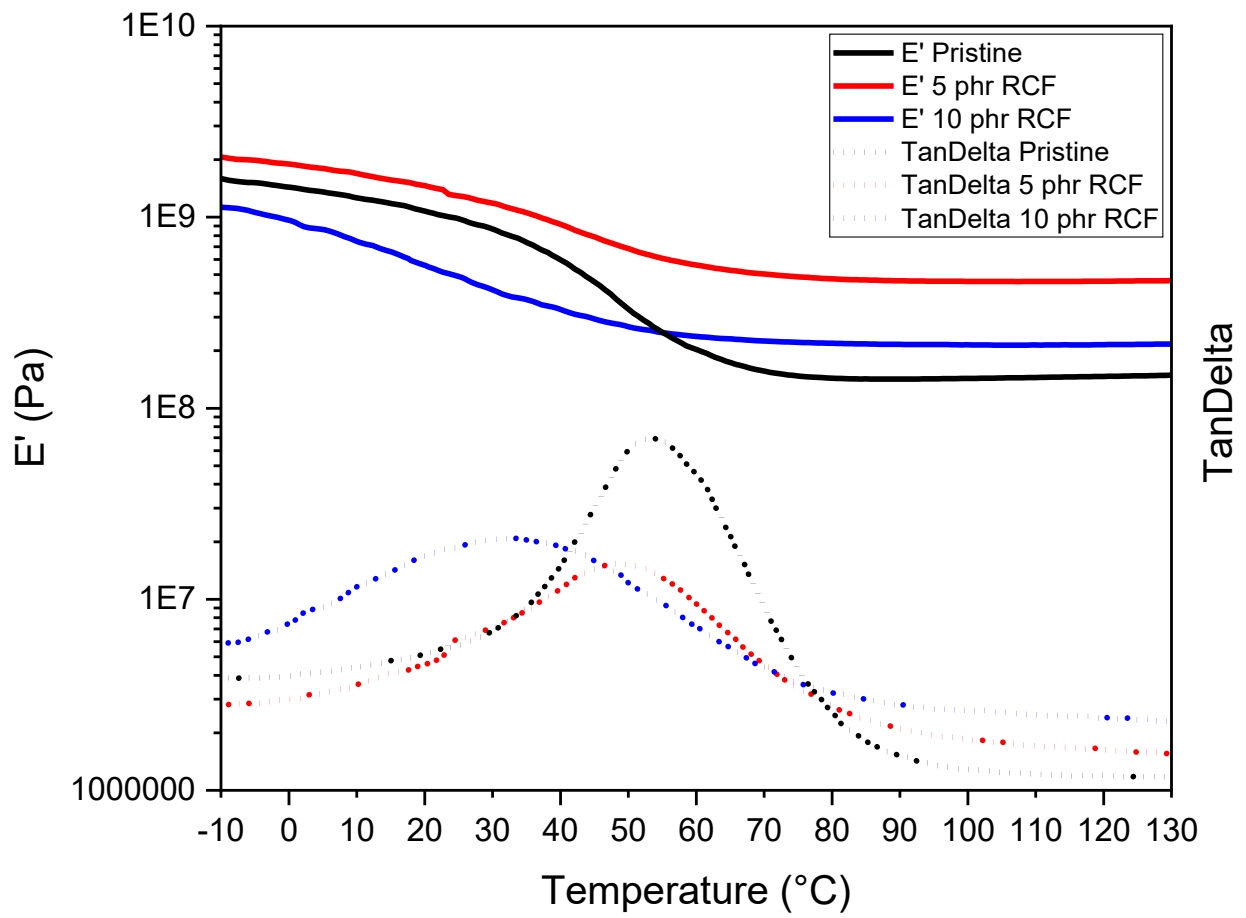
Figure 3.23: TanDelta and E' curves as a function of temperature for RCF formulations

Table 3.5 shows how the addition of various fillers, Ag, Cu, Ni, and RCF, affects the glass transition temperature T_g and the storage modulus at T_g (E' (T_g)).

Table 3.5: Values of T_g and E' (T_g) of analyzed samples

Formulation	T_g [°C]	E' (T_g) [MPa]
SA-TE12 Pristine	54 ± 1	225 ± 1
25 phr Ag	46 ± 2	257 ± 1
50 phr Ag	43 ± 1	260 ± 1
75 phr Ag	47 ± 1	239 ± 1
100 phr Ag	52 ± 2	140 ± 1
25 phr Cu	43 ± 2	255 ± 2
50 phr Cu	33 ± 2	304 ± 1
75 phr Cu	46 ± 1	280 ± 1
100 phr Cu	54 ± 2	42 ± 1
25 phr Ni	49 ± 1	306 ± 1
50 phr Ni	43 ± 2	307 ± 1
75 phr Ni	44 ± 1	349 ± 1
100 phr Ni	50 ± 2	11 ± 2
5 phr RCF	49 ± 1	708 ± 2
10 phr RCF	34 ± 1	378 ± 2

As visible from the table above, the pristine SATE12 polymer has a T_g of approximately 54°C while the addition of fillers generally lowers the Tg. For example, Cu fillers significantly reduce T_g, with the lowest value observed at 50 phr Cu around 32.8°C. However, in some cases, like with 100 phr Ni, T_g is just slightly reduced compared to lower concentrations of the same filler. However, the clear trend is a reduction of the T_g when fillers are introduced. This reduction can be attributed to the decrease of the double bond conversion, as measured from FTIR and Photo-DSC analysis, thus lowering T_g. On the other hand, at higher filler concentrations, there might be an increase in T_g, as seen with Ni. This could be since at high concentrations the filler can hinder the chain mobility of the polymeric network inducing an enhancement of T_g.

Regarding the storage modulus registered at the glass transition temperature, E' (T_g), the trend is more variable. In fact, in most cases, this value is increased, even substantially. RCF has the highest impact in enhancing the storage modulus, bringing the value from 225 MPa of the pristine sample up to 708 MPa and 378 MPa when 5 and 10 phr of RCF are introduced, respectively. However, regarding metallic fillers, sometimes the filler effect is decremental, in particular with 100 phr of Ag, Cu and Ni. As visible from the table, the most impacting drop is visible introducing 100 phr Ni, with E' (T_g) passing from 225 MPa of the pristine case down to 11 MPa.

In the case of recycled carbon fibres (RCF), the increase in E' (Tg) could be mainly due to the strong interactions between the RCF and the polymer matrix in addition with the natural rigidity of the filler itself, leading to an improvement in mechanical properties such as build-up modulus. On the other hand, metal fillers such as Ag, Cu and Ni may not disperse as well as RCF in the polymer matrix. Poor dispersion can lead to agglomeration, where particles clump together and do not contribute effectively to strengthening the material. In this case, instead of strengthening the system, agglomerates can act as defects or stress concentrators, leading to a decrease in E' (Tg). This effect

Politecnico di Torino

is particularly pronounced at higher filler loads, as in the case of 100 phr Ni, where agglomeration is more likely.

3.2.2 Tensile tests

As already introduced, through tensile testing the mechanical behavior of the 3D printed specimens was investigated. Figures from 3.24 to 3.27 show the stress-strain curves for all formulations treated, with the exception of 100 phr of Ag, Ni and Cu due to lack of biobased monomer. The reported graphs are an average calculated from three samples analyzed for each formulation.
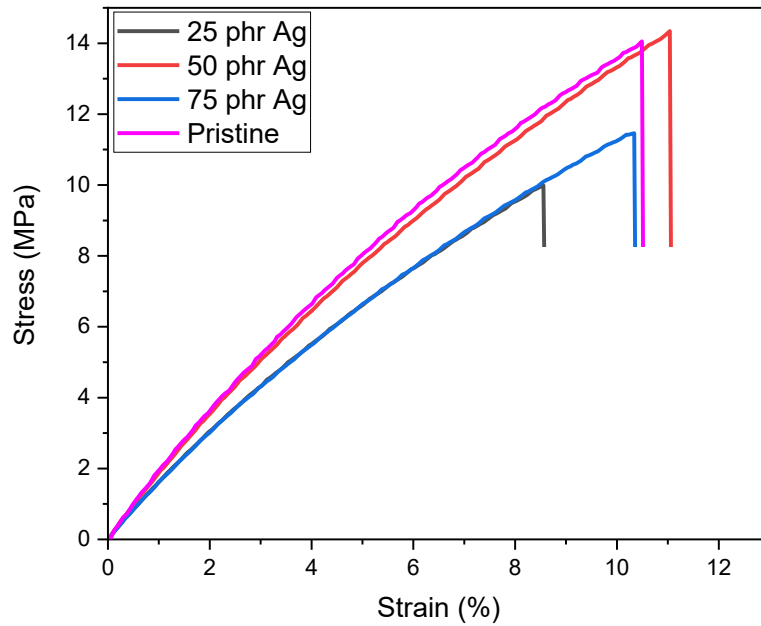

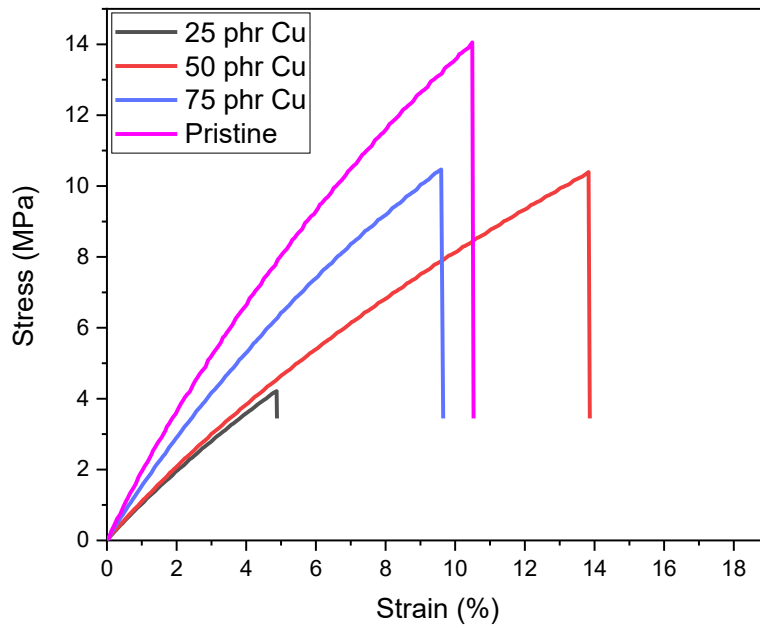*Figure 3.24: Stress vs strain curves for Ag formulations*

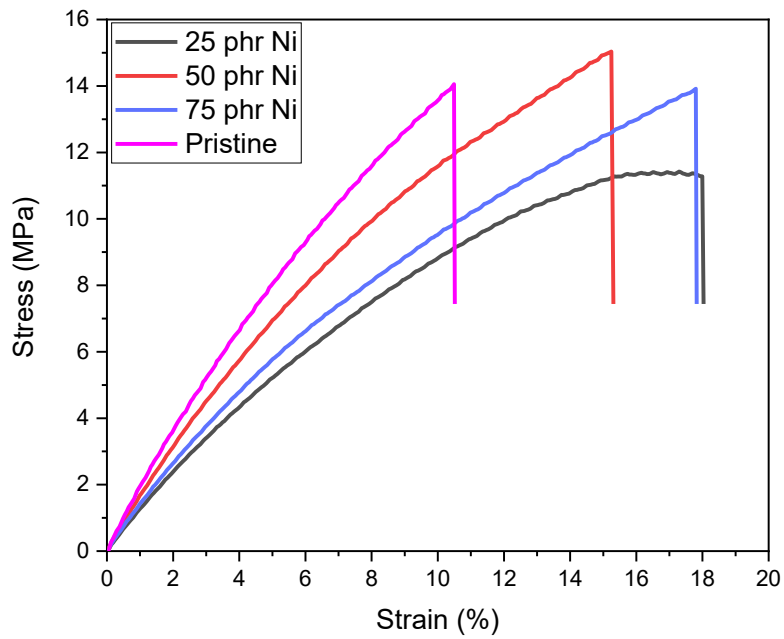*Figure 3.25: Stress vs strain curves for Cu formulations*

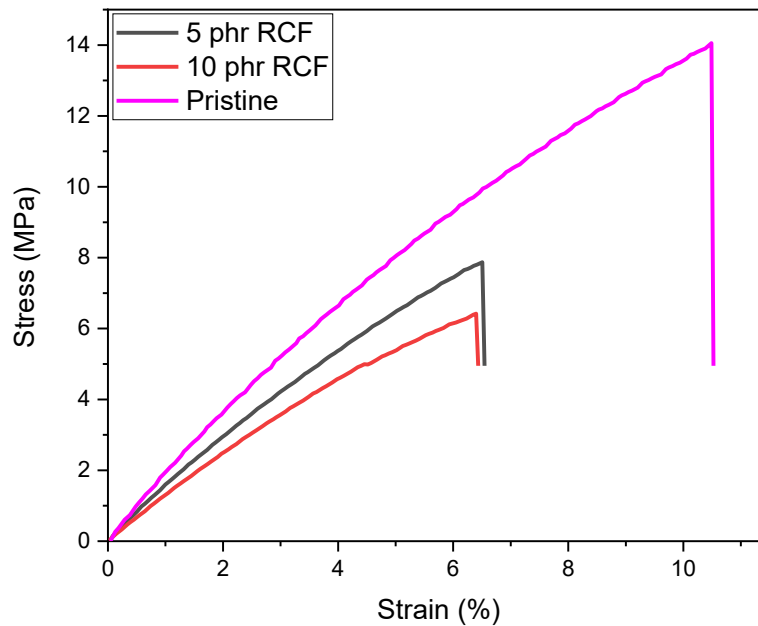*Figure 3.26: Stress vs strain curves for Ni formulations*

Figure 3.27: Stress vs strain curves for RCF formulations

Table 3.6 shows the values of Young's modulus E, rupture stress and rupture strain of each sample as an average calculated from three samples per type, analysed with standard deviation. The values of E were obtained by analyzing the first elastic section of the stress-strain curve and calculating its slope, doing this three times to obtain a standard deviation.

Table 3.6: Young's modulus, rupture stress and rupture strain of the analyzed samples

Formulation	E [MPa]	Rupture stress [MPa]	Rupture strain [%]
SA-TE12 Pristine	1,7 ± 0,1	12,0 ± 3,1	11,7 ± 1,6
25 phr Ag	1,4 ± 0,2	9,1 ± 1,9	9,3 ± 2,4
50 phr Ag	1,6 ± 0,1	14,9 ± 1,1	11,9 ± 1,2
75 phr Ag	1,4 ± 0,1	11,5 ± 1,9	10,2 ± 0,5
25 phr Cu	0,9 ± 0,1	4,1 ± 0,6	4,5 ± 0,9
50 phr Cu	1 ± 0,0	10,7 ± 3,1	13,4 ± 3,7
75 phr Cu	1,4 ± 0,1	11,1 ± 1,0	10,6 ± 0,9
25 phr Ni	1,1 ± 0,2	12,7 ± 1,3	19,3 ± 2,0
50 phr Ni	1,4 ± 0,2	14,2 ± 3,6	14,4 ± 4,0
75 phr Ni	1,1 ± 0,2	13,4 ± 1,5	15,2 ± 2,9
5 phr RCF	1,4 ± 0,1	8,5 ± 1,3	7,9 ± 1,5
10 phr RCF	1,2 ± 0,1	6,7 ± 0,2	6,2 ± 0,5

As reported in the table above, the samples composed by pristine SA-TE12 polymer exhibit an elastic modulus of 1,72 MPa. It's possible to notice that the addition of fillers generally reduces the modulus across all the formulations. Cu fillers have the most pronounced effect, with the modulus dropping significantly for 25 and 50 phr Cu with a value approximately of 0,9 and 1 MPa respectively, indicating very poor reinforcement. On the other hand, Ag, Ni and RCF fillers show a more moderate effect, with modulus values slightly lower but still comparable to the pristine polymer, suggesting a relatively good interaction with the matrix.

Additionally, the rupture stress shows very varying trends depending on the filler type and concentration. Again, Cu fillers drastically lower the most rupture stress at 25 phr (4,1 MPa), pointing to poor mechanical reinforcement at lower concentrations. However, at higher Cu concentrations (50 and 75 phr), the rupture stress still reduced but more slightly. Additionally, RCF fillers reduce consistently the rupture stress too, especially at 10 phr (6,7 MPa). This generic trend can be potentially due to filler agglomeration and, in the case of RCF, badly oriented, generating a weak bonding with the matrix. This hypothesis is substantiated by the FESEM images, reported in Figures 3.28, 3.29, 3.30. In particular, Figure 3.28 and Figure 3.29 shown a marked agglomeration and bad dispersion of Ag and Ni powder (50 phr), respectively, while Figure 3.30 reported the random orientation of the carbon fibers (5 phr) in the polymeric matrix.

Regarding rupture strain, the pristine polymer has a value of 11,7%. Generally, all the fillers approximately maintain or slightly reduce rupture strain, indicating that the composite's ductility is largely preserved. However, Cu filler shows a significant decrease in strain at 25 phr (4,5%), indicating increased brittleness. Additionally, Ni fillers stand out for significantly increasing rupture strain, particularly at 25 phr (19,3%), which suggests that these composites are more ductile and capable of withstanding more deformation before rupture. In contrast, RCF fillers lead to a notable reduction in rupture strain, with the lowest observed at 10 phr (6,2%), indicating a shift towards a more brittle material with limited elongation.
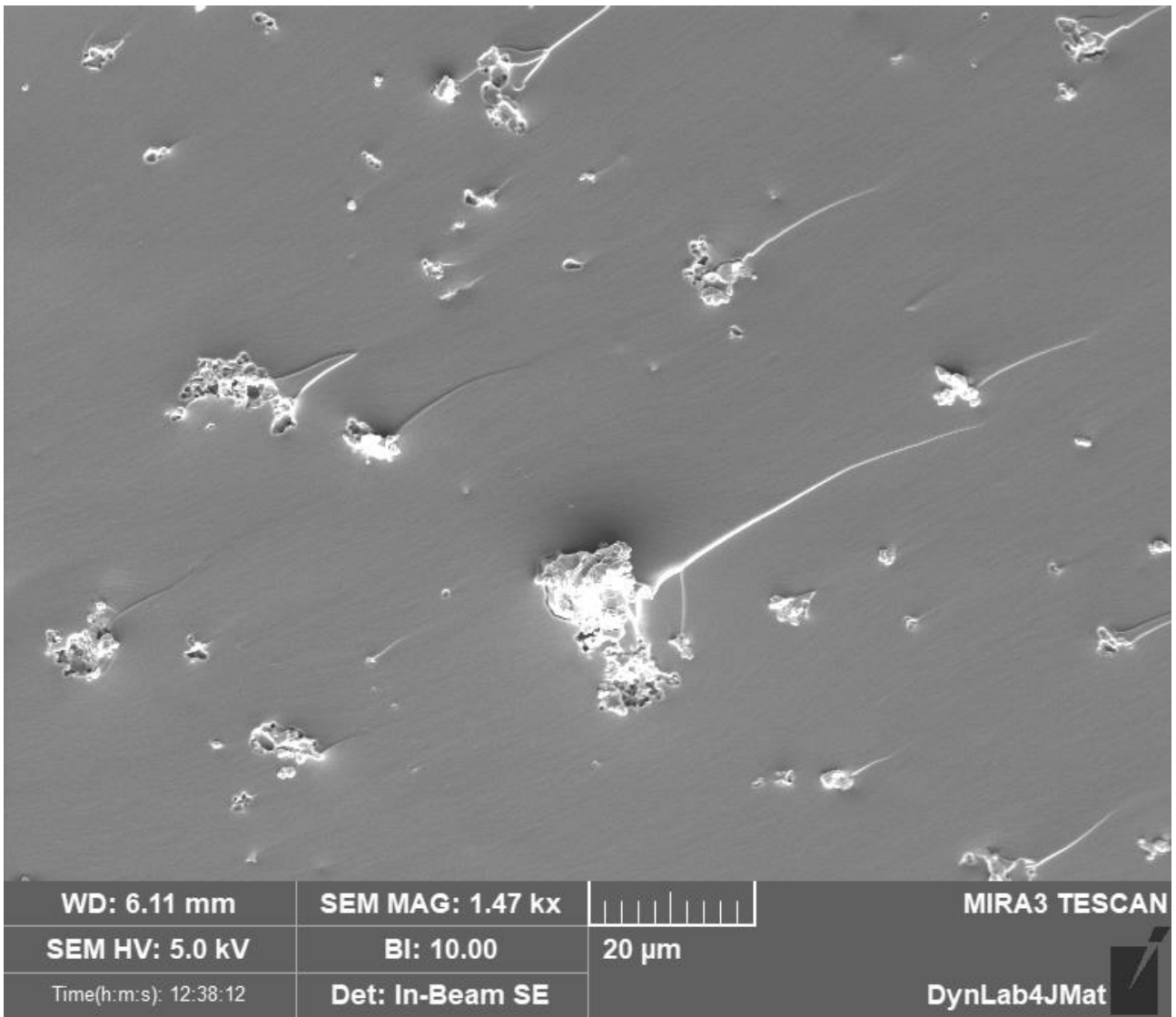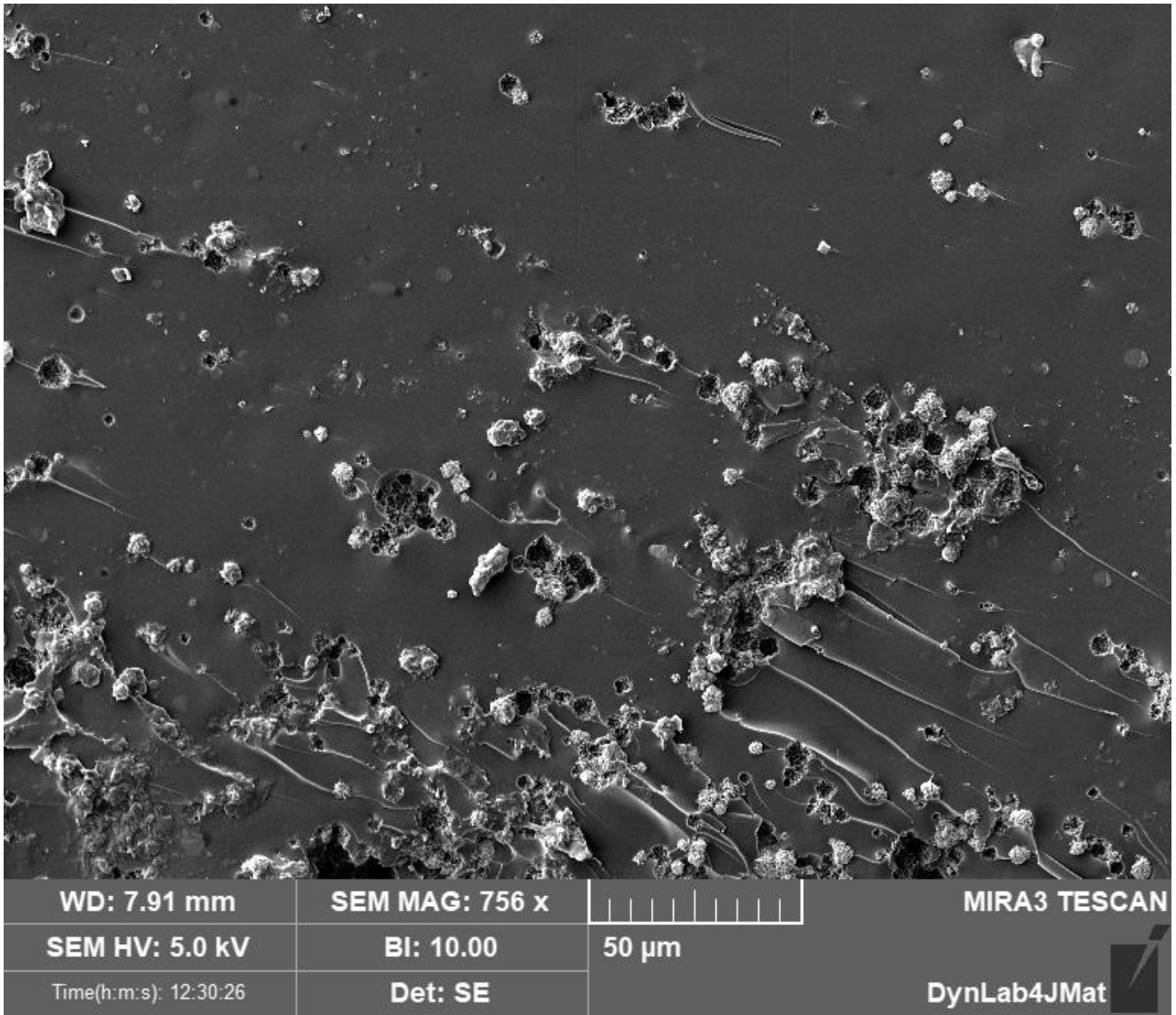
Politecnico di Torino

Figure 3.28: FESEM image showing the agglomeration of silver powder in the SA-TE12 matrix

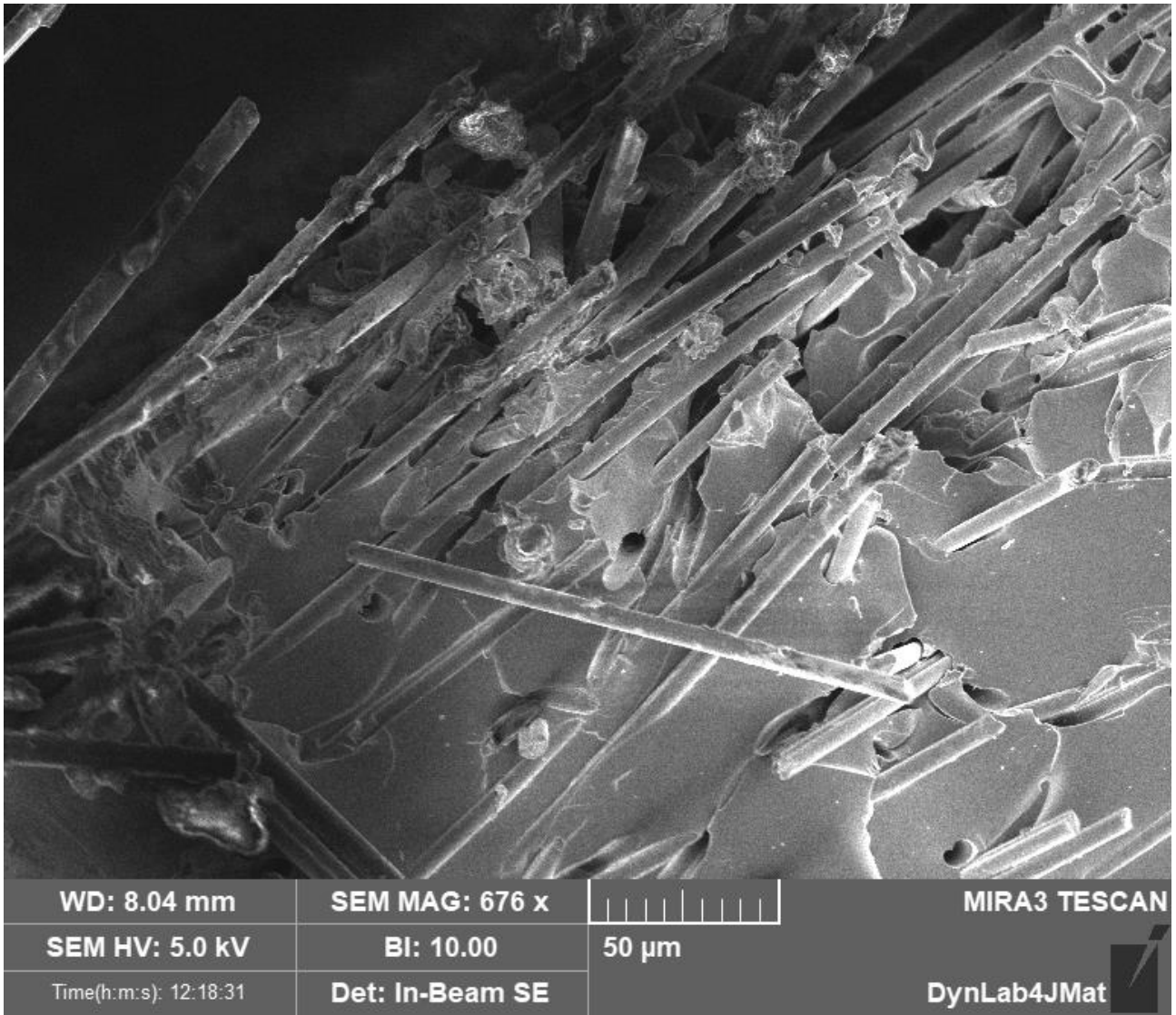*Figure 3.29: FESEM image showing the agglomeration of nickel powder in the SA-TE12 matrix*

Politecnico
di Torino

Figure 3.30: FESEM image showing the random orientation of RCF in the SA-TE12 matrix

3.2.3 Electrical conductivity and Joule effect

As already mentioned in section 2.5, electrical conductivity and Joule effect characterizations were conducted at Universidad Rey Juan Carlos Campus de Móstoles in Madrid, Spain.

The electrical conductivity of all the formulations as a function of the filler content is shown in Figure 3.31 and it was obtained using Equation 2 reported in section 2.5.4.
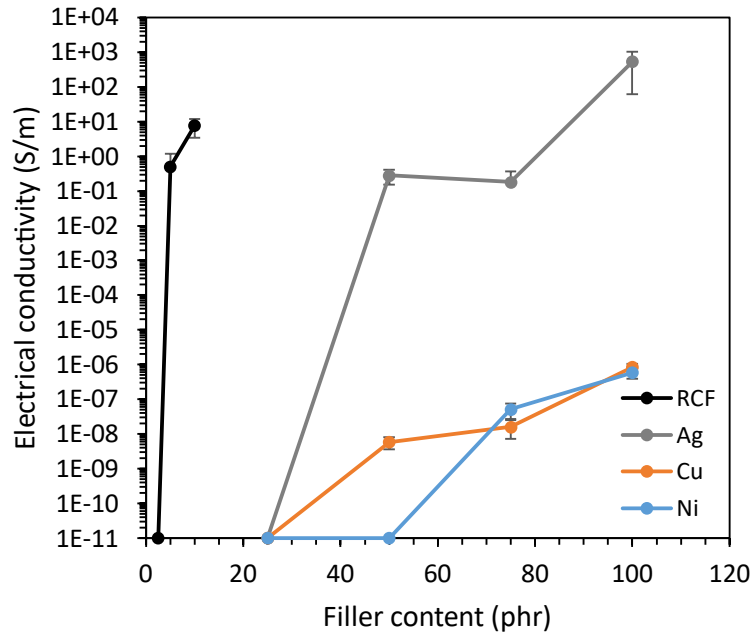

Figure 3.31: Electrical conductivity as a function of filler content and type

The specimens containing RCF reached the electrical percolation threshold using just 5 phr of filler, followed by the specimens reinforced with Ag and Cu (around 50 phr), and finally, the ones reinforced with Ni (around 75 phr). Moreover, from the graph above it is noticeable that the highest conductivity was achieved by the 100 phr Ag due to the high filler content and the excellent conductivity of Ag.

In this regard, it is worth mentioning that the results obtained with the RCF are quite interesting, since this conductive filler comes from waste, which promotes sustainability, it is way cheaper than the other fillers, and a low amount is needed to reach the electrical percolation threshold.

On the other hand, Joule heating is directly related to the electrical conductivity, as shown in Figure 3.32(a). Here, the higher the electrical conductivity, the higher the temperature reached by Joule heating.

By analyzing the results in detail, just the specimens containing RCF or Ag were able to increase the temperature by Joule heating, due to their higher electrical conductivity in comparison to the ones reinforced with Cu or Ni. In fact, these specimens did not increase the temperature despite applying even 500-600 V, in comparison to the 1-10 V applied to Ag and RCF specimens. As result, Cu and Ni specimens have been discarded. Nevertheless, two conditions showed the best results for in terms of heating, basically due to their higher electrical conductivity. These are the 10 phr RCF, reaching temperatures over 60 °C by applying around 10 V, and the 100 phr Ag, which reached temperatures over 60 °C with just 1 V.

Furthermore, Figure 3.32(b) shows the homogeneity in Joule heating (H), that can be calculated using Equation 3, reported in section 2.5.4.

Here, the specimens that presented a higher electrical conductivity and, therefore, higher Joule heating capability, also showed a higher H. This can be explained because these contents are above the electrical percolation threshold. On the other hand, the specimens near the electrical percolation threshold present regions that are locally more electrically conductive, and other regions that are not percolated, leading to a higher heterogeneity in Joule heating. In this sense, Figure 3.32(c) shows thermographs of the specimens at the maximum applied voltage of each manufacturing condition, which are in total agreement with the results obtained in terms of homogeneity in Joule heating.
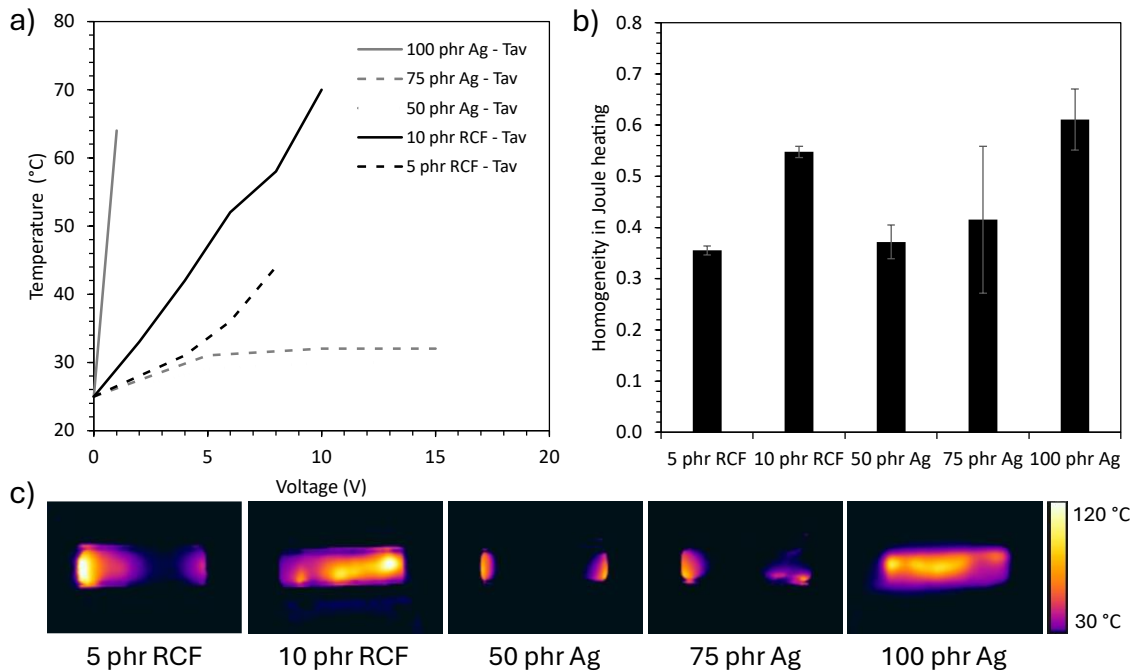

Figure 3.32: Temperatures achieved by Joule heating for different samples as a function of applied voltage (a), homogeneity of Joule heating for different samples (b), thermographs of samples at maximum applied voltage (c)

In addition, a Joule heating test was conducted on the proof-of-concept rings for thermotherapy, to investigate the influence of geometry on the electrical performance of the sample. Once more, silver paste and copper electrodes were positioned on opposing flat surfaces to induce Joule heating through the rings. As illustrated in Figure 3.33(a), the silver-containing ring exhibited an excellent behavior, attaining average temperatures of approximately 60°C when subjected to a limited voltage of 1-3 V. However, the RCF ring was unable to be heated by the Joule effect despite the utilization of higher voltages, as evidenced in Figure 3.33(b). This can be attributed to the random distribution and larger size of the filler, which impede the formation of the electrical percolation network through the ring. Furthermore, the print resolution is inferior when RCF is used as a filler, mainly due to the larger size of the fibers, which increases the probability of non-adhered layers or void zones.
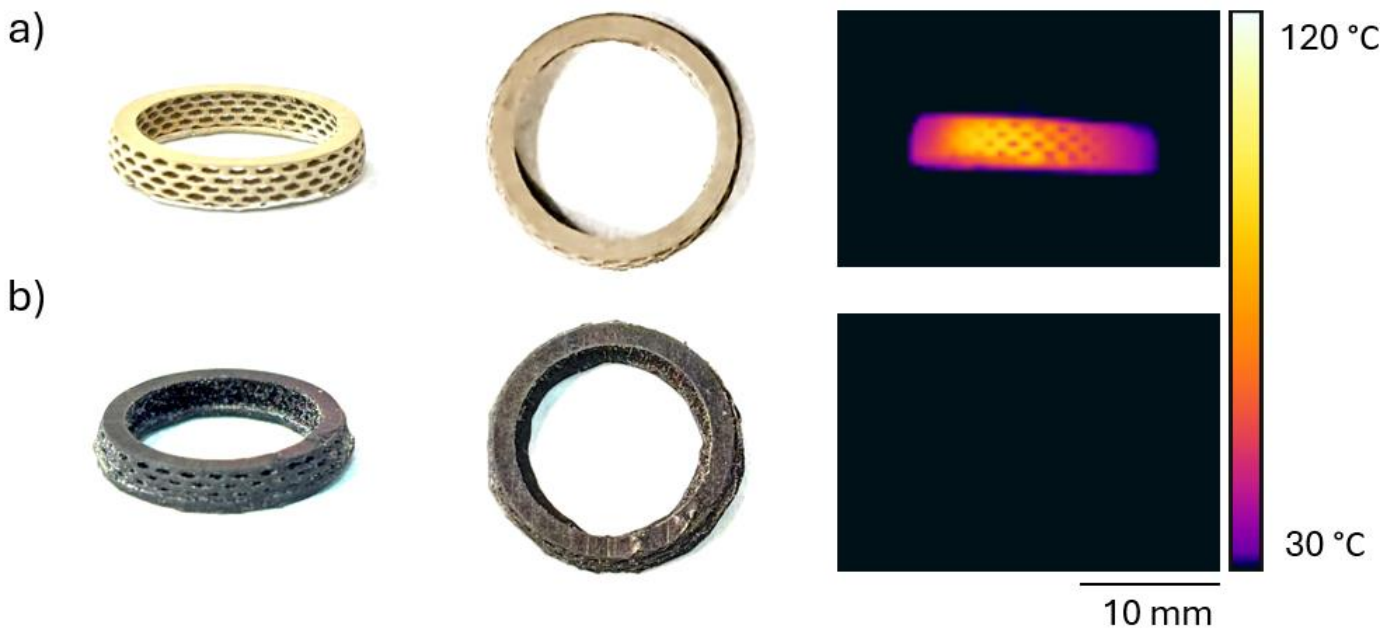
Figure 3.33: Joule heating tests carried out for the proof-of-concept honeycomb rings.
a) 100 phr Ag, b) 10 phr RCF
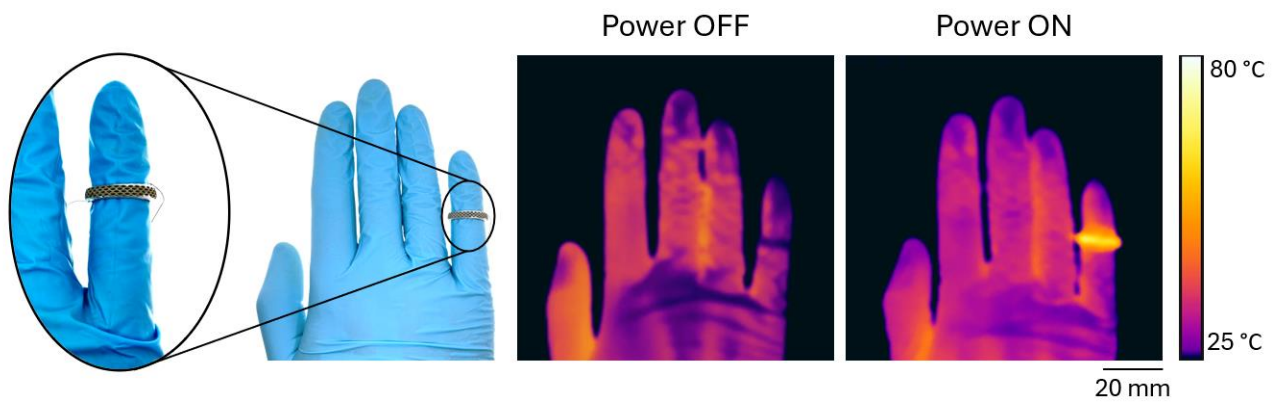
Figure 3.34: Performance of the proof-of-concept ring with 100 phr of Ag powder

Therefore, the performance of the silver ring is illustrated in Figure 3.34 while the device is worn on a finger. It should be emphasized that the object could be 3D printed with all kinds of geometries and shapes to properly fit the different phalanges of a hand or to heat the desired region of the body. Considering the remarkable heating capabilities by applying low voltages and the possibility to design the device according to the patient's needs, the suitability of the developed thermotherapy devices for the proposed application was demonstrated.

4 Conclusions

This thesis focused on using biobased monomers in 3D printing to create electrically conductive materials, with the main goal of advancing sustainable manufacturing practices for functional materials. By integrating conductive fillers such as silver, copper, nickel powders, and recycled carbon fibers (RCF) into bioderived acrylate polyglycerol monomers, this study demonstrated the feasibility of producing highly conductive and eco-friendly 3D-printed geometrically complex objects, using Digital Light Processing (DLP) technology.

In fact, the research revealed that while the addition of conductive fillers generally decreases the reactivity and increases the viscosity of the resin, increasing challenges during printing, it dramatically enhances the electrical conductivity of the printed samples. Furthermore, this grade of electrical behavior permitted to successfully exploit the Joule effect to heat up components. Among the tested fillers, recycled carbon fibers stood out as a particularly promising option due to their sustainability, cost-effectiveness, and ability to achieve electrical percolation at relatively low concentrations. However, some problems arose when switching to complex geometries, which disrupted electrical percolation and thus did not allow heating by the Joule effect. In this case, the best material proved to be resin with 100 phr Ag, reaching high temperatures (60°C) while applying low voltages (1-3 V).

Summing up, the possibility to 3D print electrically conductive structures opens new doors in fields such as electronics, where custom-designed conductive pathways can be integrated into devices, and in the medical sector, where it was proven in this study that these materials could be effectively used for thermotherapy applications by exploiting Joule heating.

Future works could explore further optimization of the resin formulations, scaling up the printing process, and investigating additional applications for these conductive biobased materials, in particular regarding the medical sector. Overall, this thesis provides a solid foundation for the continued development of sustainable and functional materials in the field of additive manufacturing.

Politecnico di Torino

5 References

1. Rosenboom, J.-G.; Langer, R.; Traverso, G. Bioplastics for a Circular Economy. Nat. Rev. Mater. 2022, 7, 117–137.
2. Unni, A.B.; Joseph, T.M. Enhancing Polymer Sustainability: Eco-Conscious Strategies. Polymers 2024, 16, 1769.
3. Malanga, G.A.; Yan, N.; Stark, J. Mechanisms and Efficacy of Heat and Cold Therapies for Musculoskeletal Injury. Postgrad. Med. 2015, 127(1), 1–9.
4. Yi, G.Y.; Kim, M.J.; Kim, H.I.; Park, J.; Baek, S.H. Hyperthermia Treatment as a Promising Anti-Cancer Strategy: Therapeutic Targets, Perspective Mechanisms and Synergistic Combinations in Experimental Approaches. Antioxidants 2022, 11(4), 625.
5. Shahrubudin, N.; Lee, T.C.; Ramlan, R. An Overview on 3D Printing Technology: Technological, Materials, and Applications. Procedia Manuf. 2019, 35, 1286–1296.
6. Jiménez, M.; Romero, L.; Domínguez, I.A.; Espinosa, M.d.M.; Domínguez, M. Additive Manufacturing Technologies: An Overview about 3D Printing Methods and Future Prospects. Addit. Manuf. 2019.
7. Oh, J. Recent Advances in the Reconstruction of Cranio-Maxillofacial Defects Using Computer-Aided Design/Computer-Aided Manufacturing. Maxillofac. Plast. Reconstr. Surg. 2018, 40(1).
8. Ávila, L.A.; Graf, B.; Rehmer, B.; Petrat, T. Characterization of Ti–6Al–4V Fabricated by Multilayer Laser Powder-Based Directed Energy Deposition. Adv. Eng. Mater. 2024, 24(6).
9. Chen, N.; He, C.; Pang, S. Additive Manufacturing of Energetic Materials: Tailoring Energetic Performance via Printing. J. Mater. Sci. Technol. 2022, 127, 29–47.
10. 3D Hubs. How to Design Parts for Material Jetting 3D Printing. 3D Hubs. Available online: https://www.3dhubs.com/knowledge-base/how-design-parts-material-jetting-3d-printing (accessed on [insert access date]).
11. Parchegani, S.; Piili, H.; Ganvir, A.; Salminen, A. Laser Welding of Additively Manufactured Parts - A Review. IOP Conf. Ser. Mater. Sci. Eng. 2023, 1296(1).
12. Dudek, P.; Rapacz-Kmita, A. Rapid Prototyping: Technologies, Materials and Advances. Arch. Metall. Mater. 2016, 61(2).
13. Pateloup, V.; Michaud, P.; Chartier, T. Optimization of Part Orientation and Adapted Supports for Manufacturing of Ceramic Parts by Stereolithography Using Finite Element Simulations. Open Ceram. 2021, 6, 100132.
14. Zhang, F.; Zhu, L.; Li, Z.; Wang, S.; Shi, J.; Tang, W.; Li, N.; Yang, J. The Recent Development of Vat Photopolymerization: A Review. Addit. Manuf. 2021, 48, 102423.
15. Salame, P.H.; Ananya, N.; Haran, H.S.; Pillai, S.R.; Kulsange, B. Multicomponent and Multimaterials Medical Additive Manufacturing. In Medical Additive Manufacturing: Concepts and Fundamentals; Additive Manufacturing Materials and Technologies, 2024; pp. 563–597.
16. Zakeri, S.; Vippola, M.; Levänen, E. A Comprehensive Review of the Photopolymerization of Ceramic Resins Used in Stereolithography. Addit. Manuf. 2020, 35, 101177.
17. Sekmen, K.; Rehbein, T.; Johlitz, M.; Lion, A. Thermal Analysis and Shrinkage Characterization of the Photopolymers for DLP Additive Manufacturing Processes. Continuum Mech. Thermodyn. 2022, 36(4).
18. Johnson, A.R.; Caudill, C.L.; Tumbleston, J.R.; Bloomquist, C. Single-Step Fabrication of Computationally Designed Microneedles by Continuous Liquid Interface Production. PLOS ONE 2016, 11(9).
19. Rad, Z.F.; Prewett, P.D.; Davies, G.J. High-Resolution Two-Photon Polymerization: The Most Versatile Technique for the Fabrication of Microneedle Arrays. Microsyst. Nanoeng. 2021, 7, 71.

20. Pazhamannil, R.V.; Govindan, P. Current State and Future Scope of Additive Manufacturing Technologies via Vat Photopolymerization. Mater. Today Proc. 2021, 43(1), 130–136.
21. Amini, A.; Guijt, R.M.; Themelis, T.; De Vos, J.; Eeltink, S. Recent Developments in Digital Light Processing 3D-Printing Techniques for Microfluidic Analytical Devices. J. Chromatogr. A 2023, 1692, 463842.
22. Chekkaramkodi, D.; Jacob, L.; Shebeeb, M.C.; Umer, R.; Butt, H. Review of Vat Photopolymerization 3D Printing of Photonic Devices. Addit. Manuf. 2024, 86, 104189.
23. Ballard, N.; Asua, J.M. Radical Polymerization of Acrylic Monomers: An Overview. Prog. Polym. Sci. 2018, 79, 40–60.
24. Cramer, N.B.; Bowman, C.N. Thiol-Ene and Thiol-Yne Chemistry in Ideal Network Synthesis. In Polymer Chemistry Series; Materials and Nanoscience Subject Collection; RSC Publishing, 2013; pp. 1–27.
25. Wang, H.; Jin, Z.; Hu, X.; Jin, Q.; Tan, S.; Mahdavian, A.R.; Zhu, N.; Guo, K. Continuous Flow Cationic Polymerizations. Chem. Eng. J. 2022, 430(2).
26. Fertier, L.; Koleilat, H.; Stemmelen, M.; Giani, O.; Joly-Duhamel, C.; Lapinte, V.; Robin, J.-J. The Use of Renewable Feedstock in UV-Curable Materials – A New Age for Polymers and Green Chemistry. Prog. Polym. Sci. 2013, 38(6), 932–962.
27. Biermann, U.; Bornscheuer, U.; Meier, M.A.R.; Metzger, J.O.; Schäfer, H.J. Oils and Fats as Renewable Raw Materials in Chemistry. Angew. Chem. Int. Ed. 2011, 50(17), 3854–3871.
28. Hanganu, B.; Velnic, A.-A.; Ciudin, V.P.; Crauciuc, D. The Study of Natural Saponification Processes in Preservation of Human Corpses. Rev. Chim. 2017, 68(12), 2948–2951.
29. Goyal, S.; Hernandez, N.; Cochran, E.W. An Update on the Future Prospects of Glycerol Polymers. Polym. Int. 2021, 70(7).
30. You, A.-R.; Kim, J.-Y.; Ryu, S.-W. Synthesis of Acrylate-Functionalized Polyglycerols and an Investigation of Their UV Curing Behaviors. ChemistrySelect 2023.
31. le Duigou, A.; Castro, M.; Bevan, R.; Martin, N. 3D Printing of Wood Fibre Biocomposites: From Mechanical to Actuation Functionality. Mater. Des. 2016, 96, 106–114.
32. Kim, S.H.; et al. Precisely Printable and Biocompatible Silk Fibroin Bioink for Digital Light Processing 3D Printing. Nat. Commun. 2018, 9(1), 1180.
33. Matsukawa, K.; Miyaji, Y.; Kawabata, S. Properties of Photo-Cured Networks Using Polyglycerin Acrylates. Material Innovation Lab., Kyoto Institute of Technology, Kyoto, Japan; Sakamoto Yakuhin Kogyo, Co., Ltd., Osaka, Japan.
34. Taormina, G. Design and Characterisation of Polymeric Nanocomposites for Automotive Sector by Additive Manufacturing Technology. Ph.D. Thesis, Università di Parma, 2020. Advisor: F. Bondioli.
35. ISO 527-5:2021. Plastics — Determination of Tensile Properties — Part 5: Test Conditions for Unidirectional Fibre-Reinforced Plastic Composites; International Organization for Standardization, 2021.

Acknowledgments

I would like to thank Professor Marco Sangermano for the cultural and emotional support, advice and teachings he has given me during his courses, and particularly the months of thesis preparation. Thank you for dedicating so much of your time to me despite your numerous commitments.

Thanks to Lorenzo for introducing me to the laboratory and all its instruments in a precise and detailed manner. Thank you for igniting my spark for research despite our quick acquaintance. Thanks to Matteo, Matilde, Rossella and Dumitru for immediately welcoming me and making me feel like an integral part of the group from day one. Thank you for helping me with everything from bureaucratic matters to scientific questions or technical problems. Thank you also for making it possible and for sharing so many laughs and happy, unforgettable moments with me within the walls of the Poli. Thank you for taking so, so much time for me.

Thanks to Elena, Laura, Marco, Giorgio and Matteo for all the adventures we spent together during my time as a student, you are fantastic friends I can always count on. I hope to do a thousand more things with you.

Thanks to Alessio, Mario, Lennard, Miguel, Andrea and Carlota for spending time with me and making a magical Erasmus, in Grenoble and its mountains, possible.

I would like to thank my parents very much for giving me the opportunity to embark on this path and for always being there for me, supporting me with their love. I also thank my brother for putting up with me and supporting me during the toughest times for me, when I was stressed and irritable. Thank you for sharing many moments of fun and happiness with me during these five years.

Finally, I would like to thank my grandparents, who have always believed in me and supported me since I was born.

In particular, I would like to thank my grandfather Franco, for all the wise man advice he has given me over the years. He saw me start this journey and I know for sure that he is by my side even at this moment of conclusion. I will never forget your affection and your words. Throughout my life I will try to have your strength, determination and mentality as a Marina Militare rower. I dedicate this achievement to you.

As I am writing these words, my grandmother is in the operating theatre for an operation on her shoulder and elbow. I hope she recovers soon and well, so that we can return to the garden together and help her in the kitchen, making jams, sauces and fresh pasta.

Politecnico di Torino